DESIGN AND TEST OF A DETECTOR FOR CHARGE READ-OUT IN TMBI

BACHELOR THESIS

Nils Marquardt

Westfälische Wilhelms-Universität Münster
Institut für Kernphysik
AG Weinheimer

First Referee: Prof. Dr. C. Weinheimer
Second Referee: Prof. Dr. K. Schäfers

Declaration of Academic Integrity

I hereby confirm that this thesis on **Design and test of a detector for charge readout in TMBi** is solely my own work and that I have used no sources or aids other than the ones stated. All passages in my thesis for which other sources, including electronic media, have been used, be it direct quotes or content references, have been acknowledged as such and the sources cited.

_____

(date and signature)

I agree to have my thesis checked in order to rule out potential similarities with other works and to have my thesis stored in a database for this purpose.

_____

(date and signature)

Contents

1 Introduction

In recent times, medical imaging became a very powerful and important tool in the examination of the human body. One technique used is the positron emission tomography (PET). It is based on the simultaneous detection of two photons indirectly generated by a radiopharmaceutical in the patients body. The first detector for positron emission tomography was built by James Robertson in 1961 [1]. Since then, various detector models have been designed and built, improving the resolution of the derived images.

The BOLD-PET (Bismuth Organometallic Liquid Detector) project is a collaboration of the Institut für Kernphysik, the EIMI (European Insitute for Molecular Imaging) of the WWU Münster and the CaLIPSO-group (Calorimetre Liquide Ionisation Position Scintillation Organometallique) of the CEA Saclay. It aims to build a liquid ionization detector for the simultaneous detection of the ionization current produced by high-energy photons, and the Cherenkov light emitted from relativistic photoelectrons in the liquid. The liquid used is the organometallic trimethylbismuth (TMBi) with a bismuth mass fraction of 82 %. Since bismuth with an atomic number of 83 has the highest cross section for the photoelectric effect of all stable isotopes, nearly 50 % of the times the 511 keV-photons deposit their energy in the liquid through the photoelectric effect, making it suitable as a medium for a PET detector[2].

The objective of this bachelor thesis is the design of a detector with which currents in TMBi can be measured. In the first section, the physical processes involved in the imaging in positron emission tomography are described. In the following, two different PET detector variants are presented, the commonly used scintillation detector and the approach of this work, the liquid ionization detector. The third section explains the design and setup of the newly built detector. The next section is then dedicated to the measurements with it. Current measurements are carried out in vacuum and in the liquid from which the corresponding capacitances of the detector are derived. From these in turn an estimate for the relative permittivity of trimethylbismuth can be derived for which there is no value in literature yet. In the end the results will be summarized and an outlook for future measurements with the liquid is given.

2 Principles of positron emission tomography

Positron emission tomography is a versatile nuclear imaging technique that finds many applications in medicine e.g. in diagnosing diseases like Alzheimer's or cancer. The patient is injected with a chemically active molecule that is radioactively labeled (tracer). One of the most commonly used tracers is fluorodeoxyglucose (FDG), a glucose analog that behaves almost exactly like glucose and participates in the metabolism of the body. Tracers used for PET are positron emitters with short half-lives to minimize the radiation patients receive. After a given time, the radioactive distribution within the patient is measured and from this, information about the tracer distribution is drawn. In the case of FDG, this allows for the determination of areas with high metabolic activity.

2.1 β^+-decay

The β^+-decay as seen in fig. 1 is fundamental to PET. Inside the nucleus of the positron emitting isotope ${}^{A}_{Z}\mathrm{X}$ of the radiotracer, with the mass number A and atomic number Z, a proton (p) converts into a neutron (n). In this process, a positron (e^+) and an electron-neutrino (ν_e) are emitted, decreasing the atomic number by one, thus changing the element to ${}^{A}_{Z-1}\mathrm{Y}$. Therefore, the equation can be written for the atoms as

$$ {}^{A}_{Z}\mathrm{X} \longrightarrow {}^{A}_{Z-1}\mathrm{Y} + \mathrm{e}^+ + \nu_\mathrm{e} \tag{1} $$

or in case of the proton as

$$ \mathrm{p} \longrightarrow \mathrm{n} + \mathrm{e}^+ + \nu_\mathrm{e}\,. \tag{2} $$

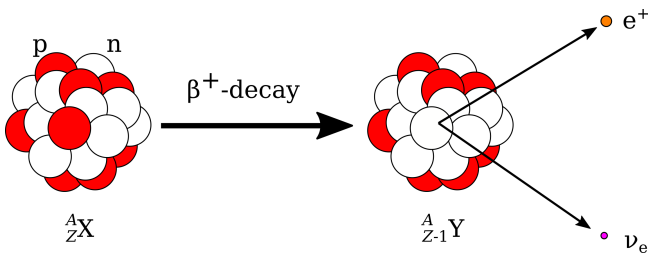

Figure 1: Schematic representation of the β^+-decay: a proton of the element ${}^{A}_{Z}\mathrm{X}$ converts into a neutron, emitting a positron and an electron-neutrino and changing the element to ${}^{A}_{Z-1}\mathrm{Y}$.

It should be noted that the β^+-decay can not happen outside of an atom due to the higher mass of the neutron compared to the proton[1]. Therefore, this decay can only happen when energy is given to the proton and is not possible for free protons. In atoms, this energy can be provided by the binding energy of the nuclei if the absolute binding energy of the nucleus in ${}^{A}_{Z-1}\mathrm{Y}$ is greater than the one of ${}^{A}_{Z}\mathrm{X}$. The released energy in this decay is split between the positron, the neutrino and the nucleus of ${}^{A}_{Z-1}\mathrm{Y}$. Therefore, the energy distribution of the decay is continuous and the energies of the particles is not fixed, but only limited by a maximum end point energy. The nucleus can be left in an excited state which descends into lower states through emission of photons (γ) with discrete energy, until it reaches the ground state.

[1] $m_\mathrm{n} = 939.565\,420\,52\,(54)\,\mathrm{MeV}/{c_0}^2$, $m_\mathrm{p} = 938.272\,088\,16\,(29)\,\mathrm{MeV}/{c_0}^2$ [3]

2.2 Positronium

After the decay, the neutron stays in the nucleus while the positron and the neutrino are emitted. While the positron, due to scattering, loses energy to the surrounding tissue and thermalizes, the neutrino most likely escapes the body without interaction. The thermalized positron then can either directly annihilate with an electron (less than 2% of the time [4]) or form a bound state with it, the positronium (see fig. 2). Since electrons and positrons are fermions with spin $s = 1/2$, the total spin S of the bound state can either be zero or one. In the singlet state with $S = 0$ the spins of positron and electron are anti-parallel. This state is called para-positronium and has a lifetime in vacuum of 0.125 ns [5]. The triplet state with $S = 1$ and parallel spins is called ortho-positronium and has a lifetime of 142.05 ns [5]. Both states can convert into each other through spin flip interactions with their surrounding. In the

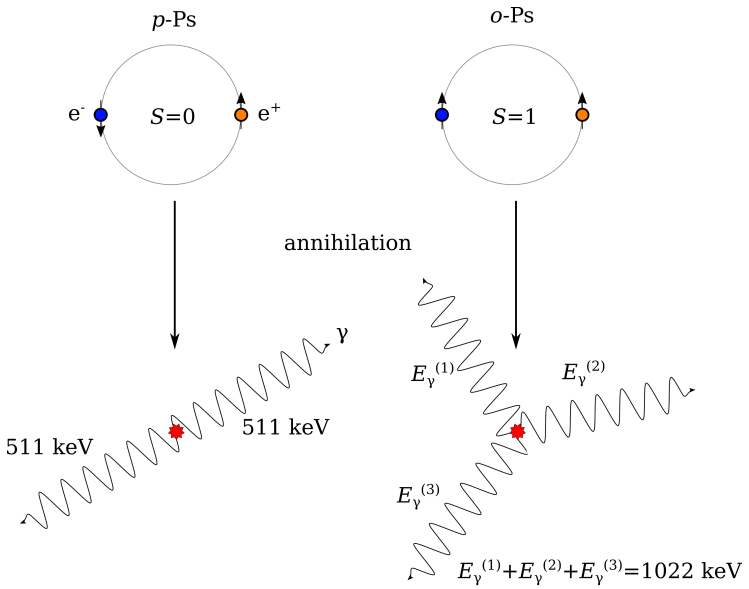

Figure 2: Schematic representation of the two forms of the positronium: para-positronium (p-Ps) has a spin of 0 and decays into two back-to-back photons with each 511 keV, ortho-positronium (o-Ps) has a spin of 1 and annihilates into three photons where the energy of 1022 keV splits statistically.

annihilation, an energy of 1022 keV, the combined rest energies of the electron and positron, becomes free in the form of photons, which are bosons with spin $s = 1$. Because of momentum and angular momentum conservation, the ortho-positronium must annihilate into an uneven amount and at least three photons. The released energy is then shared statistically between them [6]. Para-positronium on the other hand annihilates into an even number of photons, most likely two. Decays of ortho- and para-positronium with more than two photons only account for 0.003 % of all annihilations [7]. The two-photon-case is also the decisive one for PET. In this case, the energy splits equally between the two photons, which then each have an energy of 511 keV and are emitted in an angle of 180° apart. If the para-positronium carries a momentum at its decay, the photons will not be exactly emitted back-to-back, but with a distribution of angles around 180°. This distribution can be approximated by

a Gaussian with a full width at half maximum (FWHM) of about 0.5° [7]. This effect is called noncolinearity.
The emitted photons can undergo various interactions with the surrounding matter before they leave the patient and reach the detectors. Differentiating between these interactions is crucial for a high contrast in the images produced in PET.

2.3 Photon interaction with matter

Since the 511 keV-photons are the particles to be detected in PET, it is important to know how they interact with matter (surrounding tissue, air, detector material). In general, the intensity $I(x)$ of a beam of photons after the distance x within a medium can be described by the exponential function

$$I(x) = I_0 \exp\left(-\mu x\right), \tag{3}$$

where I_0 is the ingoing intensity and μ the linear attenuation coefficient. The higher the coefficient, the more photons interact with the medium. The attenuation length is given by $1/\mu$, the distance at which the intensity of the ingoing beam is reduced to $1/\mathrm{e}$ ($\approx 36.79\%$). μ is composed of the coefficients of individual interaction processes that can occur: $\mu = \sum_i \mu_i$. The individual coefficients μ_i can be derived from the cross sections σ_i of the processes (which are depicted in fig. 3) using the relation

$$\mu_i = \frac{\rho}{m_A}\sigma_i \tag{4}$$

with ρ being the density and m_A the atomic mass of the material. In general, the cross sections of the occurring processes are dependent on the material and the photon energy.

Rayleigh scattering

Rayleigh scattering (fig. 4), also called coherent scattering, is the scattering of a photon on an atom without losing energy. The photon interacts with an electron of the atom and stimulates vibrations with the same frequency as its own. The electron thus becomes an electric dipole and radiates light with the frequency of the vibration, which has the same frequency as the ingoing photon as shown in fig. 4. Since the frequencies, and therefore the energies, are the same, the process can be described by scattering of the ingoing photon. The cross section σ_{Rayleigh} of Rayleigh scattering for photon energies $E_\gamma > 10\,\text{keV}$ can be described by

$$\sigma_{\text{Rayleigh}} \propto \frac{Z^{5/2}}{A \cdot E_\gamma^2} \tag{5}$$

with Z being the atomic number and A the mass number of the scattering atom [9].

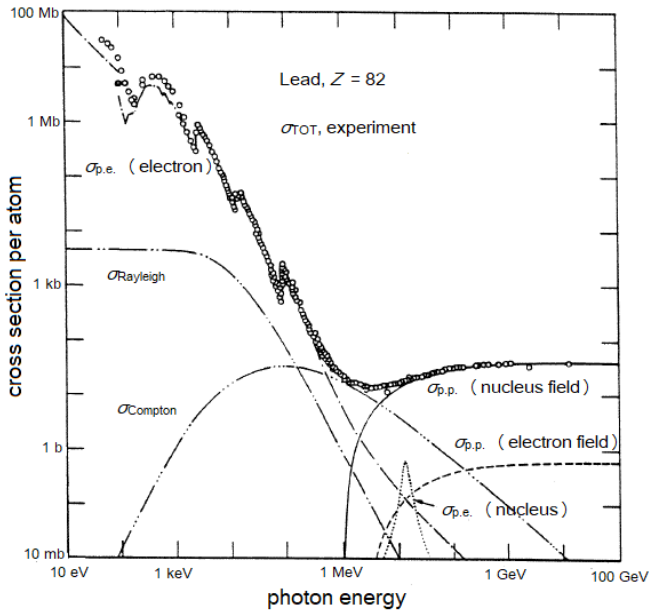

Figure 3: The measured total cross section σ_{TOT} in barns per atom ($1\,\mathrm{b} = 10^{-28}\,\mathrm{m}^2$) plotted against the photon energy in eV for lead. The curves represent the contribution of the different effects to the total cross section: Rayleigh scattering $\sigma_{\mathrm{Rayleigh}}$, photoelectric effect $\sigma_{\mathrm{p.e.}}$ on an electron and on the nucleus, Compton scattering $\sigma_{\mathrm{Compton}}$ and pair production $\sigma_{\mathrm{p.p.}}$ in the field of a nucleus and electron, respectively. The figure is taken from [8].

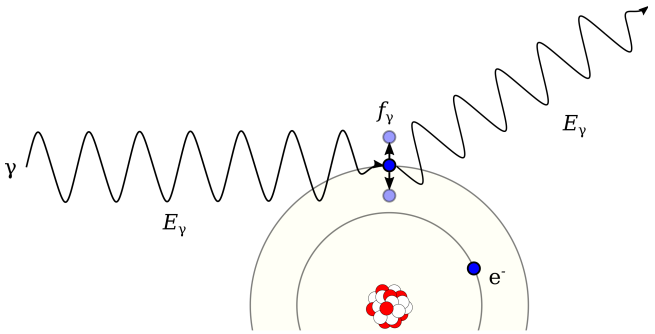

Figure 4: Schematic representation of Rayleigh scattering: a photon with the frequency f_γ and the energy $E_\gamma = h \cdot f_\gamma$ (h is the Planck constant) stimulates an oscillation of a bound electron with the same frequency which then in turn emits a photon with the energy and frequency of the ingoing photon.

Photoelectric effect

In the photoelectric effect (fig. 5), the photon disposes all of its energy to an orbital electron of an atom. For this effect to occur, the energy E_γ of the photon has to be greater than the binding energy B of the electron. The electron then escapes the atom with a kinetic energy $E_{e^-} = E_\gamma - B$. The resulting hole in the shell of the atom is filled by an electron of a higher shell under emission of a photon with an energy equal to the difference between the shells. For the cross section $\sigma_{\text{p.e.}}$ of the photoelectric effect the relation

$$\sigma_{\text{p.e.}} \propto \frac{Z^5}{E_\gamma^{7/2}} \tag{6}$$

is valid [10]. The cross section is not continuous as it shows resonances. At these, the photon energy allows to ionize a new shell, as seen in fig. 3.
Similar to the photoelectric effect is the nuclear photoabsorption. In this effect, the photon is absorbed by the nucleus of the atom and one or more nuclei are ejected. Since the nuclear photoabsorption typically occurs between a photon energy of 6 to 20 MeV [9] it can be neglected for PET.

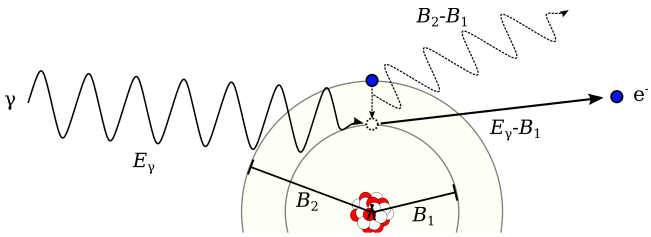

Figure 5: Schematic representation of the photoelectric effect: a photon disposes its energy to a bound electron which is emitted from the atom with an energy of $E_\gamma - B_1$, where B_1 is the binding energy of the electron. Another electron with a higher binding energy B_2 then can fill the hole left by the photoelectron, under emission of a photon with the energy $B_2 - B_1$.

Compton scattering

Compton scattering (fig. 6), also called incoherent scattering, occurs between the photon and a free or loosely bound electron. The photon thereby loses part of its energy and changes direction. The energy E'_γ of the photon after scattering is given by

$$E'_\gamma = \frac{m_e c_0^2}{\frac{m_e c_0^2}{E_\gamma} + 1 - \cos(\theta)} \tag{7}$$

with m_e the electron mass and θ the scattering angle of the photon varying between 0° (no scattering) and 180° (back scattering). The electron gets an energy of $E_{e^-} = E_\gamma - E'_\gamma$. Using $E_\gamma = 511\,\text{keV}$ from the annihilation of the positron and electron and the maximal scattering angle $\theta = 180°$, eq. (7) leads to a minimal energy of the scattered photon of $E'_\gamma = 170\,\text{keV}$, corresponding to a maximal electron energy

$E_{e^-} = 341\,\text{keV}$. This value is called the Compton edge. The cross section σ_{Compton} for Compton scattering follows

$$\sigma_{\text{Compton}} \propto \frac{Z}{E_\gamma}. \tag{8}$$

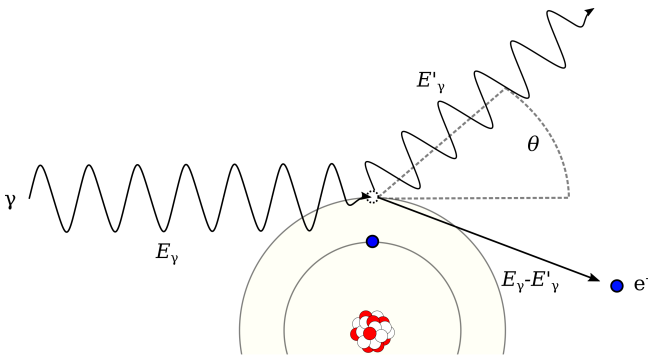

Figure 6: Schematic representation of Compton scattering: a photon scatters on a free or losely bound electron, changing its direction by the angle θ and decreasing its energy. The electron gets the difference of the photon energy before and after the scattering.

Pair production

Another process, which can be neglected for PET but shall nevertheless be explained for the completeness of the photon-matter-interactions, is pair production (fig. 7). The pair production can be seen as the inverse of the electron-positron annihilation since in this effect an electron-positron pair is generated out of a photon. For this to happen, the photon has to have at least an energy of 1.022 MeV, the combined rest energy of the electron and positron, and it has to be in the Coulomb field of an atomic nucleus. The process can also happen in the electric field of a bound electron, where the electron gets accelerated through recoil energy and leaves the atom, thus also called triplet production. The probability for pair production in the electron field is approximately 10^3 less than in the nucleus field [10]. The cross section $\sigma_{\text{p.p.}}$ of the pair production near the nucleus has the form [11]

$$\sigma_{\text{p.p.}} \propto Z^2 \ln(E_\gamma). \tag{9}$$

If the process happens in the electron field, the proportionality in the atomic number changes from quadratic to linear [12]. Since the threshold energy for pair production is two times greater than the energy of a photon produced in the positron-electron-annihilation, this process should not appear in PET. An exception is when the nucleus of the end product in the β^+-decay is in an excited state which then emits a photon with an energy higher than the threshold.

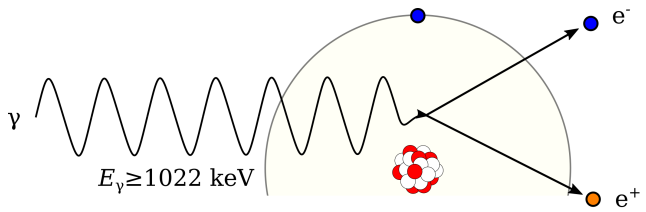

Figure 7: Schematic representation of pair production in the nucleus field: a photon in the Coulomb field of an atomic nucleus with an energy of at least 1022 keV produces an electron and a positron.

2.4 Localization of the annihilation

An accurate localization of the radiotracer through the detection of the back-to-back emitted 511 keV-photons produced in the annihilation of positronium is of great importance for PET. Therefore, the detector, or rather the detector material, should have a high detecting efficiency for those photons. For PET-detectors, the efficiency is given by the attenuation length $1/\mu_{\text{p.e.}}$ of the photoelectric effect [13]. Because the photon pairs are emitted back-to-back and no spatial direction is distinguished, multiple detectors are needed to detect pairs coincidentally and cover the whole space. The detectors can be arranged stationary in a ring (2D-image) or tube (3D-image) around the patient, or opposite groups of detectors can revolve around the subject.
When a coincident photon pair is detected by two of the detectors, one can draw a line between them, the so called line of response (LOR). Along this line the annihilation of the positronium must have happened. Since the annihilation generally does not occur in the center of the LOR, the photons travel different distances and arrive at different times at the detectors. Because of this a coincidence window must be established, that is the difference in time between the detection of two photons, in which they will be assigned to one annihilation. This window determines the timing resolution, where a higher resolution means a smaller window. If the timing resolution is high enough (< 1 ns [14]), the difference in arrival time of the two coincident photons can be used to narrow the point of annihilation further down along the LOR. This is called time-of-flight (TOF) resolution.
The accuracy with which the position of the radiotracer can be determined is called the spatial resolution. The size of the detectors facing the subject affects the spatial resolution with which the position of the radiotracer can be located. A smaller detector size contributes to a better resolution. However, the localization of the radiotracer, and thus the spatial resolution, has a finite limit due to the distance the positron/positronium travels before thermalization/annihilation. This range depends on the energy of the positron and the surrounding material. Another parameter that affects the resolution is the size of the detector ring. Due to the noncolinearity effect (section 2.2), a greater radius R leads to a deviation from the annihilation site which per geometry is given by $\tan(0.25°) \cdot R \approx 0.0044R$ (FWHM) [15]. The radius and the detector size also contributes to the parallax effect. This effect occurs when the annihilation is not located in the center of the detector ring. If the annihilation happens in the center of the detector ring, the photons enter the detectors at normal incidence. Otherwise, if the annihilation occurs at a radial offset, the photons can enter the detectors at different angles. Then it is possible that, if the

photon does not interact with the detector it first enters, the photon is detected by an adjacent detector. The LOR is then mispositioned because it is drawn from the face of the detector and not from the actual interaction point inside. A smaller detector size, a smaller ring radius and an offset of the annihilation site to the center all worsen the parallax effect [16]. The parallax effect can be corrected, if the detector is able to measure the depth of the photon detection, i.e. the depth of interaction (DOI).
Another obstacle in the localization of the point of annihilation is the assignment of LORs that do not correspond with back-to-back emitted photons (true events), meaning the LORs do not represent the photon paths, as seen in fig. 8. There are multiple ways this can happen. The first are scattered coincidences. These occur when one or both photons change their path to the detector due to Rayleigh or Compton scattering. The LOR is then displaced. Because Compton scattered photons lose energy, one can differentiate between scattered and unscattered coincidences if the detector has a high energy resolution. Rayleigh scattered photons can not be distinguished since they do not lose energy. Another way to get wrong LORs are random coincidences. Those are coincidences, where two photons are detected inside of the timing window, which do not originate from the same annihilation. This leads to wrong LORs and an undesired background noise in the data. To minimize the background a small timing window is desired. It is also possible that only a single photon or more than two photons are detected in the timing window. The single photon event can happen if on its way one of the two annihilation-photons is either absorbed (photoelectric effect), or scattered (Rayleigh, Compton) out of the detection-plane. Another possibility is that the single photon stems from background outside the detector. The single photon event can be discarded as no LOR can be drawn. In the multiple photons event no clear LOR can be drawn. If n photons are detected at different detectors in the timing window, $n(n-1)/2$ LORs are possible and it is ambiguous which LOR corresponds to a true event. Depending on the evaluation method, those events are either also discarded, or in some cases, one of the LORs is randomly selected and kept [7].

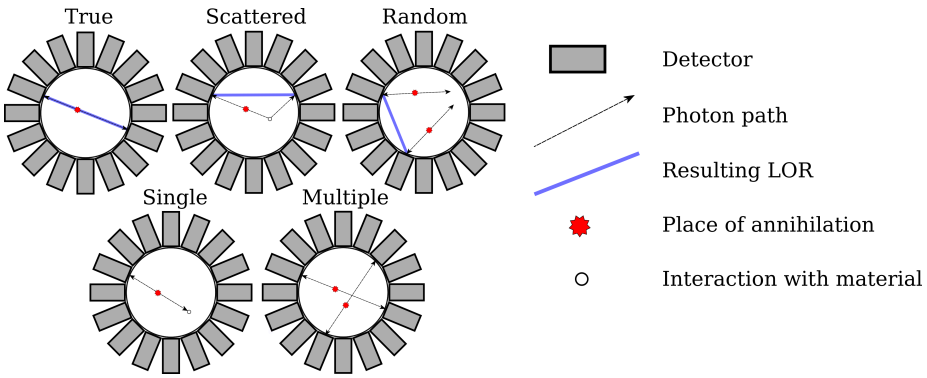

Figure 8: Schematic representation of the different types of coincidence events. A true event results in a correct LOR, in a scattered event the LOR is misplaced and in a random event a wrong line is drawn. Single and multiple events provide no or ambiguous LORs.

The number of times a LOR is drawn, or rather the number of coincidences between

the corresponding detector pair, is usually stored as an element of a matrix. The elements of the matrix are sorted in a way that the LOR in each row have the same angular orientation and in each column the same radial offset to center of the detector ring. This matrix is called sinogram. Based on the data from the sinogram there are multiple ways to reconstruct an image of the activity distribution and thus localize the annihilation site. Since this exceeds the scope of this work, reference should be made to [7, 17, 18, 19], where some algorithms such as filtered backprojection or iterative reconstruction and ways to correct the images are described in detail.

3 PET-detectors

To summarize the requirements of a PET-detector for a reconstructed, high-contrast image as mentioned in section 2.4, the following aspects are desired:

- a high cross section $\sigma_{\text{p.e.}}$/attenuation coefficient $\mu_{\text{p.e.}}$ of the photoelectric effect to ensure that the majority of the back-to-back emitted 511 keV-photons are detected and no information is lost. Therefore, detectors that are made of materials with a high atomic number Z and density ρ, having a depth of multiple attenuation lengths, are beneficial (see eqs. (3), (4) and (6)).
- a good spatial resolution to determine the position of the radiotracer. Detectors which are able to reconstruct x, y and z coordinates of the interaction inside of themselves improve the resolution.
- a timing resolution that allows to reduce the contribution of random coincidences in the image. With TOF-measurement the spatial resolution can also be improved.
- a energy resolution which allows to reject scattered coincidences, which also improves the spatial resolution.

Furthermore, when designing and building a PET-detector for commercial use in medicine, one has to keep in mind the costs and dimensions of the different parts, as they limit the utilizability of the detector. Therefore, not all aspects can typically be reached to the same degree.
In recent times, different designs for PET-detectors have been established further improving the image quality achieved in PET. In the following two designs are presented.

3.1 Scintillation detectors

Scintillation based detectors are the most commonly used detectors for PET. These detectors are made of scintillators which are coupled to photomultiplier tubes. A scintillator is a material that absorbs high-energy photons and emits low-energy photons proportional in number to the deposited energy. Depending on the material and the conversion process, it can be differentiated between organic and inorganic scintillators. For PET, inorganic scintillators in the form of doped crystals are typically used due to their high density and atomic number [7]. The emission of the low-energy photons by the crystal can be described by the band theory as depicted in fig. 9. In the crystal structure, the electron orbitals of the individual atoms overlap, forming energy bands. The highest band that is still filled with electrons is called the valence band, the band above it the conduction band and the energy discrepancy between them the band gap. The high-energy photons excite electrons from the valence band into the conduction band, creating an electron-hole-pair. Through the addition of a dopant to the crystal, defects are created in the crystal structure, the activators. The activators create energy levels in the band gap, at which the electron-hole-pairs recombine under emission of the low-energy photons. Since the energy of the emitted photons is not high enough to in turn excite other electrons, the scintillator is transparent for its emitted light. The number of photons that are produced per deposited energy is called the light output. A high light output is desired as this

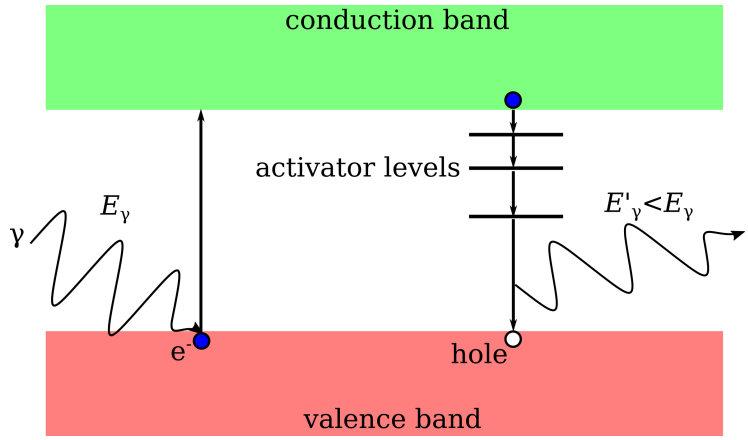

Figure 9: Schematic representation of the band structure in a scintillator: a high-energy photon excites an electron from the valence band into the conduction band, creating an electron-hole-pair. The electron and the hole can recombine at the activator levels under emission of a lower-energy photon.

correlates with a good energy resolution. Another important property of the scintillator material is the decay time. This is the time after that the light signal of the scintillator has dropped to $1/e$ of its amplitude. A short decay time is favored to distinguish fast successive coincidences and improve the timing resolution. Values of the important properties for PET for different crystal materials are listed in table 1.

Table 1: Values of the effective atomic number[2] Z_{eff}, the linear attenuation coefficient μ, the density ρ, the light output and the decay time for the common scintillator materials sodium iodide (NaI(Tl)), bismuth germanate (BGO), lutetium oxyorthosilicate (LSO) and gadolinium oxyorthosilicate (GSO). Values taken from [7] and [14].

	NaI(Tl)	GSO	LSO	BGO
Z_{eff}	51	59	66	74
μ [1/cm] at 511 keV	0.34	0.70	0.88	0.96
ρ [g/cm^3]	3.67	6.71	7.40	7.13
light ouput [photons per 511 keV]	19400	4600	13000	4200
decay time [ns]	230	56	47	300

To convert the light signal of the scintillator crystals into a processable electric signal, photomultiplier tubes (PMTs, shown in fig. 10) are used. Due to the photoelectric effect, the low-energy photons produce electrons at a photocathode. The photoelectrons then travel to a dynode, guided by focusing electrodes and an electric field between the photocathode and the dynode. A dynode is an electron multiplying electrode at which the photoelectrons produce secondary electrons. This multiplying process is repeated several times through multiple dynodes in sequence, each at

[2] Z_{eff} is used for interaction processes that are dependent on the atomic number when dealing with compounds or mixtures of different materials. The value can be derived by different methods, for example through the mass-weighted average of the components or the interaction cross section of the material. The used method is not specified in [14].

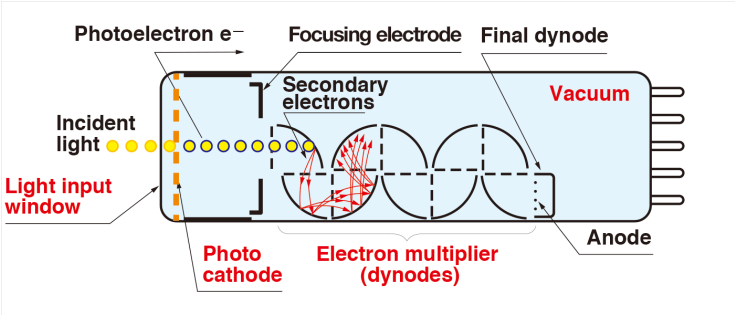

Figure 10: Schematic representation of a photomultiplier tube. The incident light produces photoelectrons at a photocathode, which are focused on dynodes where they produce secondary electrons. Through multiple dynodes the number of electrons multiplies and a current is measurable at the anode. Figure taken from [20].

a higher voltage than the one before. In this way, the number of electrons rises exponentially and at the final dynode, i.e. the anode, a current is measurable. A PMT can be characterized by its quantum efficiency and its gain. The quantum efficiency describes probability with which a photon of the incident light produces an electron at the photocathode. Typically, this probability lies between 15 and 25 %, dependent on the wavelength of the photon. The gain describes the amplification factor of the PMT. For example, if one electron produces three to four secondary electrons at a dynode, after ten steps the number of electrons and thus the gain is in the order of 10^6 [7].
Since the amplitude of the current produced by the PMT is dependent on the number of ingoing photons, which in turn is proportional to the deposited energy in the scintillator, the electric signal produced by the whole detector is dependent on the deposited energy.

3.2 Liquid ionization detectors

In contrast to scintillation detectors, liquid ionization detectors (LIDs) produce the measurable electric signal directly out of the high-energy photons and do not need the intermediate step via the scintillation light. These detectors use, as the name implies, a liquid medium to produce the electric signal through ionization. The photons ionize the atoms/molecules of the liquid and create free charge carriers. An electric field, created by the immersion of two electrodes (anode and cathode) at different voltages in the liquid, allows the electrons to drift towards the anode and the ions towards the cathode. The particles induce a charge on the electrodes, which, integrated over time, can be measured as a current. However, the induced charge is dependent on the origin position of the ionization, as electrons produced near the cathode give a longer signal than ones produced near the anode. To remove this dependency, a Frisch-grid can be added. This grid is placed at an intermediate potential between the electrodes, preferably near the anode. It causes that a charge is first induced at the anode when the electrons pass the through the grid. The ability of a liquid to produce electron-ion pairs under radiation is characterized by the free ion yield G_{fi}, the number of electron-ion pairs per 100 eV of absorbed energy. According to the Onsager theory [21], the electron and the ion can recombine if the

electron thermalizes close enough to the ion, so that the Coulomb force between them forces the recombination. Considering this effect, the free ion yield can be expressed in dependence of the electric field E by

$$G_{\mathrm{fi}} = G_{\mathrm{fi}}^{0} \cdot (1 + \alpha E)\,, \tag{10}$$

where G_{fi}^{0} denotes the free ion yield with no electric field applied. The factor α is given by

$$\alpha = \frac{e^3}{8\pi\varepsilon_0\varepsilon_r (k_{\mathrm{B}} T)^2}\,, \tag{11}$$

with e the elementary charge, ε_0 the vacuum electric permittivity, ε_r the relative permittivity (also called dielectric constant) of the liquid, k_{B} the Boltzmann constant and T the temperature. The G_{fi}-values at different electric fields can be derived measuring the current I which is induced by the source. Those quantities are connected by the relation

$$G_{\mathrm{fi}} = \frac{I}{e} \cdot \frac{100}{\Delta\epsilon} \tag{12}$$

where $\Delta\epsilon$ is the absorbed energy in the liquid per second, which is computed by Monte Carlo simulations.

The BOLD-PET project

The BOLD-PET project aims to develop a LID suitable for PET on the basis of trimethylbismuth. TMBi (Bi-$(CH_3)_3$) is an organometallic liquid with a density of $2.3\,\mathrm{g/cm^3}$ and 82 % by weight of bismuth. Since bismuth with $Z = 83$ is the heaviest stable element[3], it has the highest cross section for the photoelectric effect of non-radioactive elements and is thus well suited for PET detectors. Another useful property of TMBi is that the photoelectrons created by the 511 keV-photons are relativistic in the liquid. The photoelectrons than produce Cherenkov light, which can also be detected using photodetectors like PMTs [2].
Some important quantities regarding current and light signal, as well as the for the factor α in Onsager theory important relative permittivity, are listed in table 2 for TMBi, xenon and tetramethylsilane, liquids also used in LIDs.

[3] Bismuth is in fact not stable, but since the half-life of its most common isotope $^{209}_{83}\mathrm{Bi}$ is $1.9\,(2) \times 10^{19}\,\mathrm{yr}$ [22], this can be neglected.

Table 2: Values of the density ρ, the attenuation coefficient μ and its photo fraction, the light yield, the decay time, the zero-field free ion yield G_{fi}^0 and the relative permittivity ε_r for liquid xenon (lXe), tetramethylsilane (TMSi) and trimethylbismuth (TMBi). Value of G_{fi}^0 for lXe taken from [23] and for TMSi and TMBi taken from [24] (TMBi value is first measurement of the CaLIPSO-group). Values of ε_r are measured at −108.1 °C for lXe [25] and 20 °C for TMSi [26]. All other values taken from [2].

	lXe	TMSi	TMBi
$\rho\ [\mathrm{g/cm^3}]$	2.95	0.648	2.3
μ [1/cm]	0.28	0.063	0.40
photo fraction [%]	24	0.04	47
light yield [1/MeV]	$(1.9\text{-}4.5)\times10^5$	54-84	44-93
decay time [ns]	2.2-27 and 45	~0.1	~0.1
G_{fi}^0 [1/keV]	7.0	0.65	0.083(3)
ε_r	1.874	1.92	not measured

An advantage of TMBi over Xenon, which also has properties suitable for PET, is on the one hand the higher photo fraction of the attenuation coefficient, and on the other hand that no cryogenics are needed. TMBi has a boiling/freezing point of 105 °C/−108 °C and is thus liquid at room temperature, whereas Xenon must be cooled below −108 °C to be used in a LID, which makes it impractical for a compact detector design. However, TMBi also has a disadvantage: it is very reactant as it is selfigniting and explosive if left open at air. If just small doses of air come into contact with TMBi, the bismuth falls out as white-yellowish bismuthoxide-crystals, making the otherwise clear liquid cloudy and impure. Therefore the TMBi has to be handled with great care and it has to be ensured that no air can reach it.
Through the combined read-out of the current and the light signal it is possible to get a high spatial and timing resolution. It is estimated to reach a spatial resolution down to 1 $\mathrm{mm^3}$ and a timing resolution better than 100 ps [2].

4 Design of a new detector

The goal of this Bachelor thesis is the design and test of a new TMBi-based liquid ionization detector able to read-out a current signal. Under the absence of other gases, TMBi is in vacuum always at the verge of boiling. Small changes in temperature could lead to the formation of bubbles resulting in unwanted discharges between the electrodes, i.e. a breakdown and combustion of the liquid, damaging the detector and the electronics. In order to reduce this risk and further improve the understanding of this liquid in the presence of an electric field, three main requirements are placed on the new detector: Firstly, the liquid is pressurized to prevent boiling. This is done by an atmosphere of 1 bar argon. Secondly, the liquid filled part is transparent, allowing to monitor the TMBi and thus experiments can be stopped if bubbles form. Lastly, the volume of liquid in the detector is small (< 10 ml), to minimize damage in case of a breakdown and combustion.

Detector body

To fulfill the requirement of a see-through detector, glass is the material of choice. That is why for the TMBi-filled part of the detector, two standard CF glass-to-metal connections are used that are welded together at a right-angle, as shown in fig. 11. The glass-to-metal connections are both DN16 to keep the volume small. The right-angle form is chosen because the electrical feedthroughs needed for the anode and cathode are too large to fit through a single DN16 flange, and because it is desired to have no high voltage in the vapor phase of the TMBi. This can be achieved in the right-angle form by filling it with enough TMBi so that the horizontal glass-to-metal connection is filled entirely with the liquid. The feedthrough at the horizontal part then does not cross the vapor phase of TMBi and can be used for the high-voltage at the cathode. Because of this, a 20 kV-SHV feedthrough is used here. Accordingly, the anode feedthrough at the vertical part crosses the vapor phase, but since the anode is left at ground potential, the vapor phase does not come into contact with high voltage. Here, a BNC feedthrough is used.
The horizontal part has a length of 72 mm from the flange of the glass-to-metal connection to the welding point of the two pieces and an inner diameter of 12 mm. This value for the diameter is the largest one measured, as the diameter is not constant over the whole length: on the one hand the diameter decreases at the transition from the metal to the glass and on the other hand the diameter of the glass changes slightly due to the welding. The void volume of this cylindrical piece is thus maximum 8.14 ml. The vertical part has a maximum inner diameter of 14 mm and a flange to bottom length of 109 mm. Since this part is only filled to a level of about 3 cm, the void volume up to this level is 4.62 ml and so the total maximum void volume of both glass-to-metal connections up to a level of 3 cm is about 12.76 ml. The volume of TMBi in the detector results from the void volume minus the volume displaced by the anode and cathode. Thus, to reach a liquid volume of < 10 ml the electrodes need at least a volume of 2.76 cm^3.

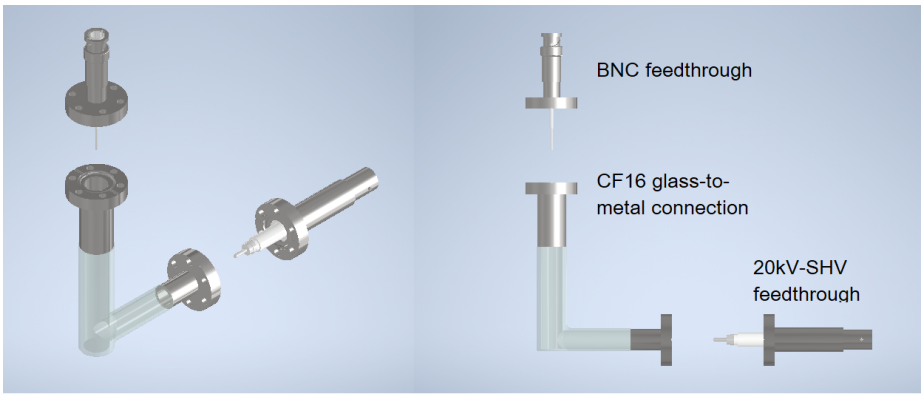

Figure 11: Models of the welded together glass-to-metal connections and the electrical feedthroughs. The 20 kV-SHV feedthrough is used for the high voltage at the cathode, the BNC feedthrough is used for the read-out of the anode. The glass-to-metal connection allows to monitor the liquid and its form prevents that high voltage crosses the vapor phase of TMBi.

Cathode

The concept for the cathode is the form of a simple round plate, like in a capacitor. However, to take up as much volume as possible, a large body is added to the plate. The material for both parts is electropolished stainless steel. The plate has a diameter of 11 mm and a thickness of 2 mm, resulting in a volume of 0.19 cm^3. The cathode body has a cylindrical shape with a diameter of 8 mm and a length of 40 mm, which gives a volume of 2.01 cm^3. The electrical feedthrough also fills in some volume since the pin is on a cylindrical ceramic isolation. This isolation has a diameter of 9 mm and a length of 20 mm, resulting in a volume of 1.27 cm^3. The total displaced volume by the cathode and the feedthrough parts is thus 3.47 cm^3.
To connect both parts of the cathode, the body has a M3-sized threaded hole on one end, and the plate the equivalent screw on one side. This also allows to change the distance between anode and cathode by simply screwing the plate further in or out. For easier handling of this, a nut is implemented between them. For the connection of the cathode with the electrical feedthrough, the cathode body has another hole on its other end, in which the pin of the feedthrough can be inserted. This connection can be locked with an M2 grub screw in the mantle of the body. A problem that now occurs is that, if voltage is applied to the cathode, high electric fields arise between the cathode body and the metal parts of the glass-to-metal connection, which are held at ground potential. To counter this, a small glass tube is pulled over the cathode body and works as an isolation. At one point, the glass tube changes its diameter, because there the diameter of the glass-to-metal connection changes due to the transition of metal to glass. This change in the tube diameter prevents it from moving, as the larger tube diameter is also larger than the smaller diameter in the glass-to-metal connection.

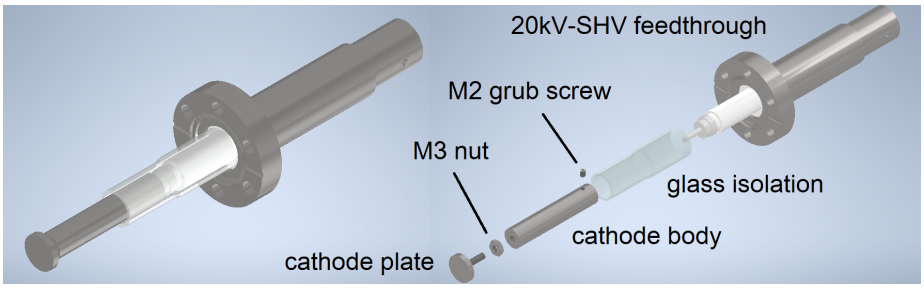

Figure 12: Model of the cathode and the electrical feedthrough. The plate can be screwed further in or out of the body, thus changing the plate distance between anode and cathode. The glass isolation protects from high electric fields between the cathode and the metal part of the glass-to-metal connection.

Anode

Like the cathode, the anode is a round plate. However, to keep the electric field between the anode and the cathode homogeneous, a guard ring is added around the plate. With just two equally sized plates, the electric field lines at the edges of the plates curve and the electric field is higher. With a guard ring at the same potential as the anode, these edge effects only occur between the cathode and the ring, leaving the field between anode and cathode homogeneous, as demonstrated by the simulations in fig. 13 performed with COMSOL Multiphysics [27]. For this to work properly, the inner diameter of the ring needs to be smaller than the diameter of the opposite cathode and the gap between ring and anode should be as small as possible. In this case, the guard ring has an inner/outer diameter of 10 mm/12 mm and the anode a diameter of 8 mm. The ring and the plate have a thickness of 1.2 mm and 4.9 mm respectively, so the volume displaced by these parts is 0.29 cm^3 in total. Since the anode is the part to read-out, it is connected with the pin of the electrical

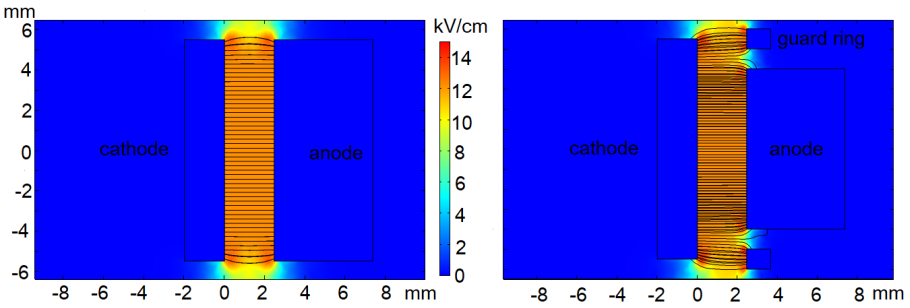

Figure 13: COMSOL-Simulations of the electric field and the field lines between the cathode at −3 kV and the anode at 0 V without guard ring (left) and with guard ring (right), at a plate distance of 2.46 mm. Without guard ring, the field lines curve at the edges of the plates, resulting in an inhomogeneous field. With guard ring, those field lines ar drawn to the ring, resulting in a homogeneous filed between anode and cathode.

feedthrough. This is done by passing a stiff wire welded to the back of the anode to

the pin, where both are connected via a terminal strip. To position the guard ring around the anode and contact it, it is welded on a metal tube, which is slipped over the wire. The tube is welded onto the electrical feedthrough with a small opening at the top to be able to reach the terminal strip. To ensure that the tube and the wire do not touch at any point, resulting in a short circuit between anode and guard ring defeating the purpose of the latter, inside the tube a smaller ceramic tube is slipped over the wire, serving as a spacer. This can be seen in fig. 14. The anode and the guard ring are thus electrically divided, since the anode is on the potential of the pin and guard ring on the potential of the shield, but both are held at 0V. The anode, guard ring, tube and the wire are all made of stainless steel and the bottom part, which comes into contact with TMBi, is electropolished.

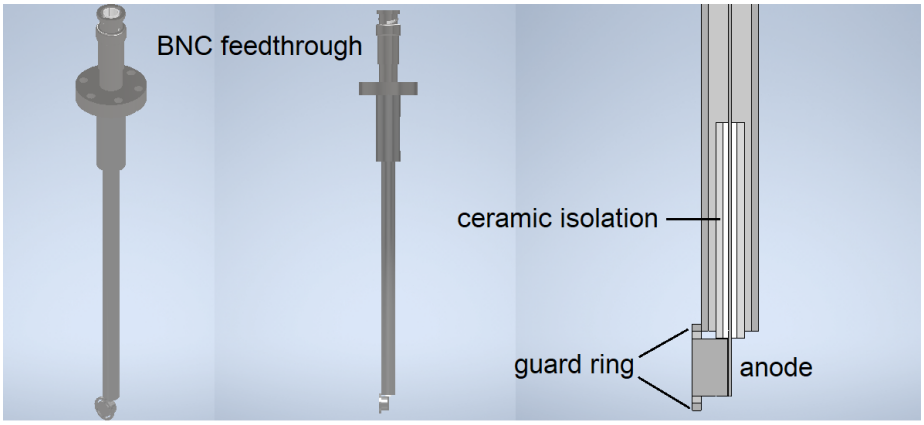

Figure 14: Model of the anode and the guard ring, connected to the electrical feedthrough. To prevent a short circuit between anode and guard ring, a ceramic isolation is placed between them.

Complete detector

Since the right angle glass-to-metal piece only has two flanges and the electrical feedthroughs also take up two flanges, a connection piece has to be added to be able to fill the detector with TMBi. Therefore, a crosspiece is inserted between the electrical feedthrough for the anode and the glass-to-metal piece, giving the possibility for two more connections. For one connection, a CF to VCR adapter is connected to an elbow, which is mounted on the detector so that the VCR adapter is facing the top. The VCR adapter is needed to connect the detector with the purification bench (see section 4) via which the filling with the TMBi and the argon is done. The other connection is used for another safety measure. Here, a bellow is added, which sits also on an elbow, so that it stands vertically. The bellow has a linear stroke of 10 mm and is closed at the top. It ensures that the detector is always at 1 bar, reducing the risk of bubble formation. A model of the complete detector and a photo of the fully assembled detector are depicted in fig. 15.
The plate distance between anode and cathode is measured to be 2.46 mm using a digital caliper. Since this value is measured from outside the detector it is only a first estimate. A more exact determination of the parameter is done in section 5.1 using the measurement of the vacuum capacitance of the detector and simulations of the

geometry in the detector. With this first estimate for the distance the active volume of TMBi is 0.12 ml, that is the volume between anode and cathode where the electric field is homogeneous. From the void volume and the volume displaced by the electrodes one gets a total TMBi volume of 9.00 ml maximum at a filling level of 3 cm. This does not include the volume displaced by the glass isolation at the cathode or by the tube and wire at the anode, so the real TMBi volume is still smaller and thus the requirement of the small volume is fulfilled.

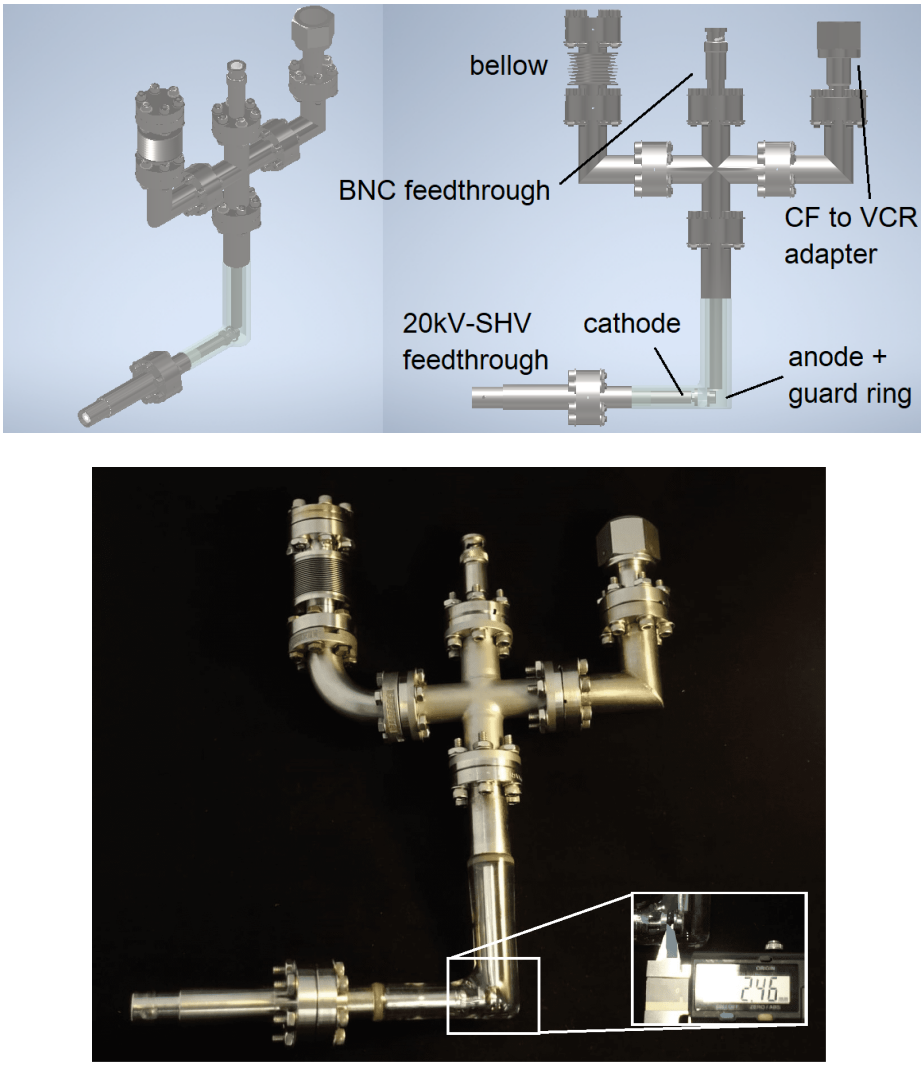

Figure 15: Model and photo of the complete detector. The bellow ensures that the pressure in the detector is always at 1 bar, the CF to VCR adapter is needed to connect the detector to the purification bench.

Experimental setup

The detector is leak tested using a Leybold PHOENIX L300i Dry leak detector [28] which gives a leakage rate of 9×10^{-10} mbar × l/s, indicating that the detector is suitable for vacuum and TMBi. The detector is then attached to a purification bench, seen in fig. 16. Via the purification bench the detector can be filled with TMBi and argon, the TMBi can be purified using Linde 4A molecular sieves and a residual gas analysis can be done using a mass spectrometer to check for impurities. As a protection against electric fields from outside, a Faraday cage surrounds the detector in the form of a closable aluminum box. For G_{fi}-measurements, a sledge is installed that is powered by a stepper motor and on which a radioactive source can be mounted, as depicted together with the aluminum box in fig. 17. This allows for an automated and reproduceable measurement of background and radiation induced current. The sledge is able to travel a total distance of 500 mm and can bring the source up to 9 mm close to the detector. The long travel path r allows to reduce the radiation proportional to $1/r^2$. The source used is caesium-137 $\left({}^{137}_{55}\mathrm{Cs}\right)$ which produces 662 keV-photons through the decay of its metastable daughter isotope barium-137m into the ground state and has an activity of 1.034 MBq (last measured on 26/02/19).

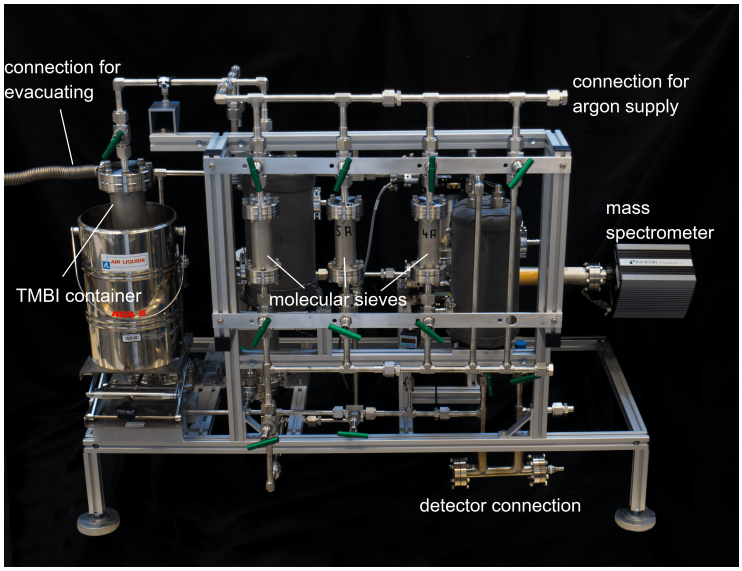

Figure 16: Photo of the purification bench as used with a previous detector (©AG Weinheimer). Since then, some modifications have been made. The molecular sieves allow to purify the TMBi. With the mass spectrometer a residual gas analysis can be done. The argon supply is not visible as it was added later. The detector depicted in this picture is an old model from previous measurements.

With the detector attached to the bench, another leak test is done, giving a leakage rate of 1×10^{-9} mbarl/s. The system is then baked-out and pumped to get out residual gases that could contaminate the TMBi, for example water. This is done at 140 °C for three days to reduce stress at the glass-to-metal connections. The sieves are baked-out at a higher temperature of 395 °C to get the substances bound in there out. The baking-out was ended at a pressure of 1×10^{-7} mbar. Before and after the baking-out a mass spectrum of the gas in the system is recorded using the mass

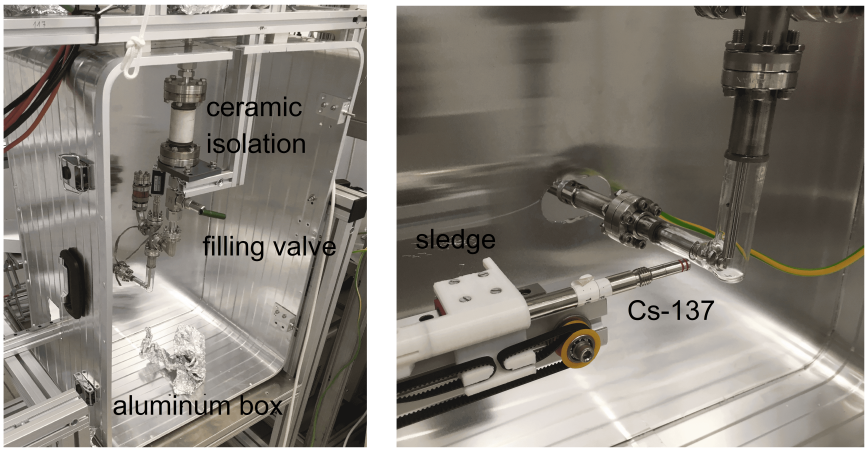

Figure 17: Photo of the aluminum box surrounding the detector (left) and the slegde for the radioactive source (right). The ceramic isolation separates the detector electrically from the bench, the filling valve allows to separate detector and bench volume.

spectrometer, a Pfeiffer PrismaPro QMG 250 M3 [29]. The spectra are shown in fig. 18. Based on the masses and their current signals in the spectrometer, water (H_2O, 18 amu) is most abundant in the system before baking-out, followed by hydrogen (H_2, 2 amu), Nitrogen (N_2, 28 amu) and carbon dioxide (CO_2, 44 amu). After baking-out, the signals of water, nitrogen and carbon dioxide are reduced by four orders of magnitude. To further compare the signals before and after baking-out, a pressure correction has to be done, in which the current signals are divided by the pressure at the spectrometer. However, since the pressure was not recorded during the measurements, this can not be done here. The reduction of the signals shows that there is no leakage in the system since nitrogen and carbon dioxide are both part of the air ($N_2 \approx 78\,\%$, $CO_2 \approx 0.04\,\%$) and would thus be measurable with their signal ratio equal to their proportion in air, if there was a leakage. The hydrogen signal is reduced by two order of magnitudes and thus still comparatively high, since hydrogen is too light to be pumped efficiently with turbomolecular pumps. A better result could be achieved with a titanium sublimation pump, but this is not needed since hydrogen is not known to react with TMBi. With the highly reduced amount of water and other residual gases, the system is ready for vacuum measurements and can then be filled with TMBi. Filling the detector is done by creating a temperature difference between detector and TMBi container. This is achieved by heating the container in a water bath and cooling the part of the bench above the detector using a LAUDA ECO RE 420 cooling thermostat [30]. The TMBi vaporizes in the container and, because of the thus produced pressure gradient between container and detector, migrates to the cooled part where it condenses and flows into the detector. When the filling level of 3 cm in the detector is reached, the inflow into the detector is stopped by closing the valve above it. The surplus TMBi in the system is pumped back into the container by reversing the temperatures of detector and container. The latter is then cut off from the system using the valve above. Before filling the detector with argon up to a pressure of 1 bar, the bench is evacuated again so that

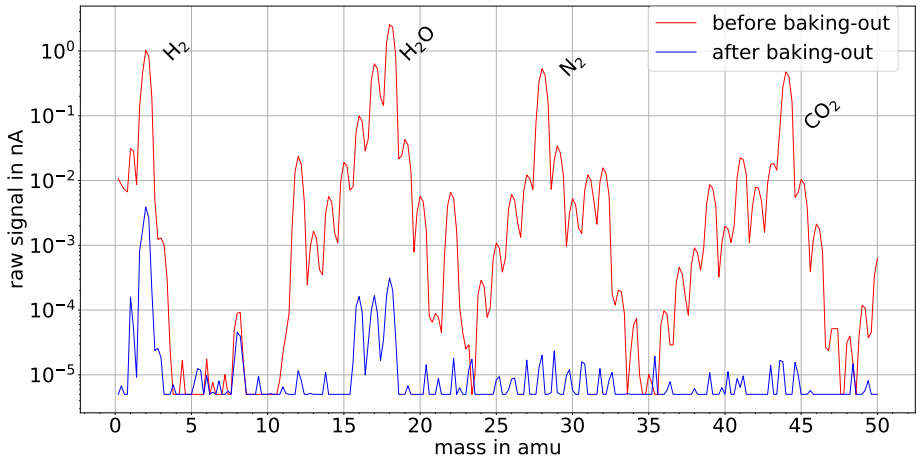

Figure 18: The measured mass spectra of the residual gas in the system, before and after baking-out. The masses are given in atomic mass units (amu) and weighted by the raw current signal of the mass spectrometer in nA.

no remaining TMBi can enter the argon bottle. By opening the valve above the detector, the argon flows inside creating the desired atmosphere over the TMBi. With the detector volume added back to the system, the pressure decreases slightly down to 941 mbar. After again closing the valve above, the TMBi-filled detector as seen in fig. 19 is ready for measurements.
The electronic needed for the current measurements and its arrangement is depicted in fig. 20. An iseg NHQ 224M [31] is used as a low-noise high voltage supply for the cathode. The voltage is controlled remotely to ensure reproducibility and can be set up to ±4000 V at voltage ramps from 2 to 255 V/s. Since the iseg is connected via SHV cable but the electrical feedthrough for the cathode needs a 20 kV-SHV cable, an adapter box is needed to connect both cables and apply the voltage at the cathode. For the read-out of the current-signal at the detector, a FEMTO DDPCA-300 current amplifier [32] is used, which can be seen in fig. 21. The amplifier is directly connected to the BNC feedthrough of the detector and is set on a rise time of 0.5 s. The amplifier is controlled and read-out remotely, therefore the transimpedance gain is set on remote and the output is short-circuited. Because of the glass part of the detector, the BNC feedthrough and therefore also the femto and the guard ring are on a floating potential. To ground those parts a cable connects the flanges of BNC and 20 kV-SHV feedthrough, thus the ground potential is provided by the iseg. Grounding the readout side of the detector also prevents possible stray capacitances of the connections from affecting the measurement. These capacitors never have the opportunity to charge and thus affect the measurement, as they are always pulled to zero by grounding.
The remote control of femto and iseg is done using LabVIEW programs running on a CompactRIO connected to the corresponding devices. This setup is used for the measurements in vacuum. For the measurements in TMBi, two more components are added. The first one is a 1 GΩ resistor between the detector and the femto. This serves as a discharge protection for the femto in the case the TMBi breaks down and a high current flows between cathode and anode. The second component is a voltage divider used to monitor the actual voltage provided by the iseg, since the

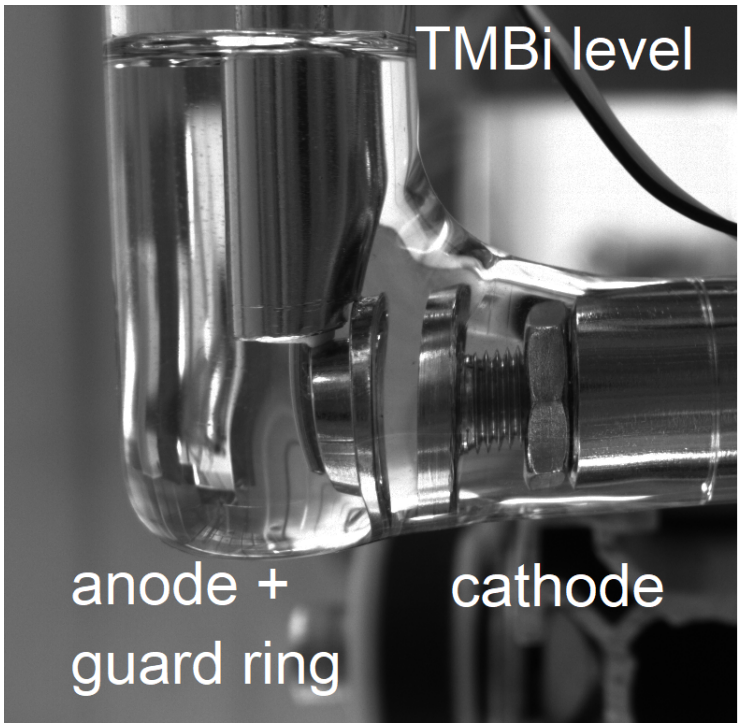

Figure 19: Photo of the detector filled with TMBi.

iseg can not be read-out directly. The reason why this is only necessary for measurements in TMBi is that in vacuum it is clearly visible from the current signal when the voltage is changed whereas in TMBi this is rather difficult. Reading-out the voltage divider is also done via the CompactRIO. By connecting all devices to the same module it is also ensured that no timing discrepancies occur in the measurements. The structure of the voltage divider is shown in fig. 22. The voltage is tapped between a 1 MΩ and a 2 MΩ resistor and is therefore a factor 500 smaller than the voltage provided by the iseg. Other combinations with higher resistors are also tested but they are found to produce noise in the signal, which is not the case with this one. The 1 GΩ resistor in the divider is added for protection of the CompactRIO against high currents in case of a breakdown.

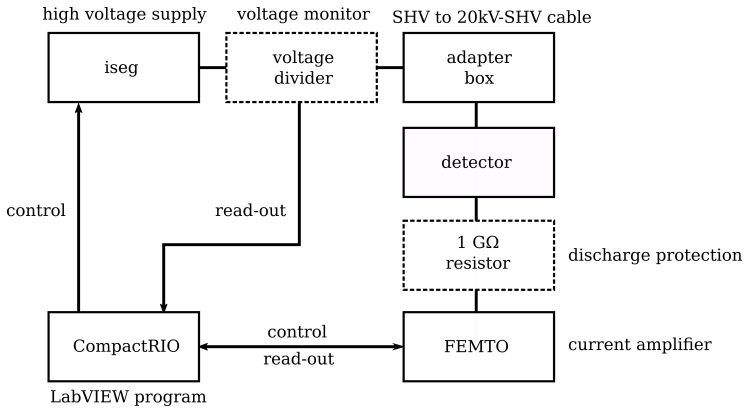

Figure 20: Sketch of the components used for the current measurements. The dashed components are only used for the measurements in TMBi.

Figure 21: The FEMTO DDPCA-300 current amplifier used to measure the current at the detector. Picture taken from [32]

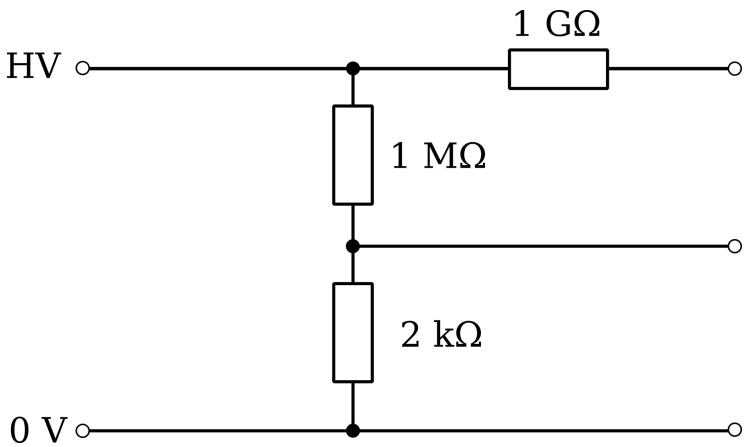

Figure 22: Sketch of the voltage divider used to measure the applied voltage via the CompactRIO. The voltage is tapped between the 1 MΩ and the 2 kΩ resistor, the 1 GΩ resistor protects the CompactRIO from high currents.

5 First measurements

The measurable current at the detector results from the relation between the charge Q and the applied voltage U at a capacitor:

$$Q = C \cdot U\,, \tag{13}$$

where the proportionality factor C is the capacitance of the capacitor/detector. The capacitance C can be described by

$$C = \Lambda \cdot \varepsilon_0 \cdot \varepsilon_r \tag{14}$$

with Λ a factor dependent on the geometry of the capacitor ($\Lambda = A/d$ for a plate capacitor with area A and distance d). Since the current I is the time derivative of the charge Q, the derivative of eq. (13) leads to

$$I = C \cdot \frac{\mathrm{d}U}{\mathrm{d}t} = C \cdot \dot{U}\,. \tag{15}$$

The current I is thus proportional to the changing rate of the voltage $\dot{U}$. Therefore, if the voltage is applied in a ramp, i.e. at a constant rate, the measured current should also be constant. Through the measurement of the current in the empty detector, i.e. in vacuum, and in the TMBi-filled detector, the capacitance can be derived for both mediums. With those values the relative permittivity $\varepsilon_r^{\mathrm{TMBi}}$ of TMBi can be derived. This follows from eq. (14) and the fact that the relative permittivity of vacuum is equal to 1. Therefore, one only needs to divide the capacitance in TMBi by the capacitance in vacuum as the geometry factor Λ falls away:

$$\varepsilon_r^{\mathrm{TMBi}} = \frac{C_{\mathrm{TMBi}}}{C_{\mathrm{vac}}}\,. \tag{16}$$

The relative permittivity is an important value for the free ion yield G_{fi} as it is part of the factor α (see eq. (11)) in the Onsager theory. Until now, no literature values for the relative permittivity of TMBi exists.

5.1 Vacuum capacitance

In vacuum, the current is measured for the ramps 2 to 20 V/s ascending in 1 V/s steps. Each time, the voltage is first changed from 0 to −500 V. After a given time, the direction of the ramp is then reversed and the voltage is set back to 0 V. Because of this, the time window where the voltage changes decreases at higher ramps. A measuring point is taken every second. The time which is waited before reversing the ramp direction and before applying a higher ramp voltage is one minute, during which background is measured. The whole measurement is done two times: first without the 1 GΩ resistor in front of the femto amplifier and then, like the measurement in TMBi, with the resistor. The reason for this is that the resistor and the detector form an RC element with the time constant $\tau = R \cdot C$, that is the time after which the capacitor reached 63.2 %/36.8 % of the charging voltage in the charging/discharging process, which could influence the measurement.
The results of the vacuum measurements are shown in fig. 23. It is visible that each time a voltage ramp is applied, the current leaps to a higher value and stays constant, as it was expected. When going up to −500 V the sign of the current is negative, when

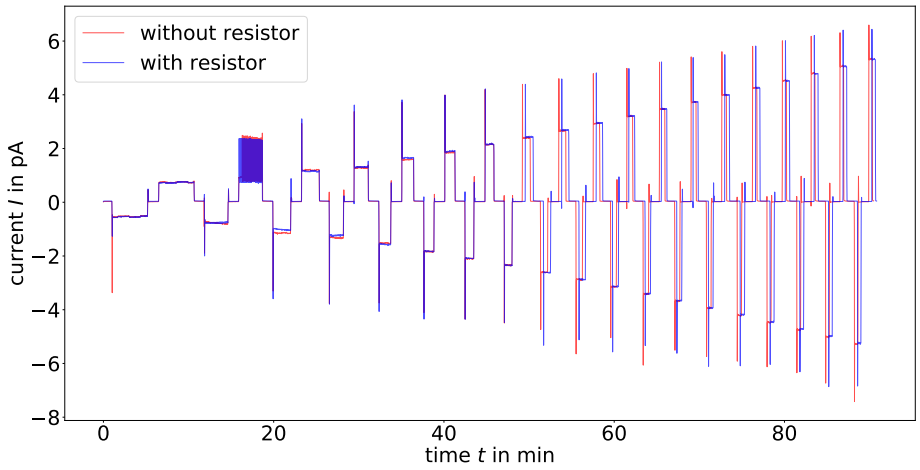

Figure 23: Measurement of the current at the detector in vacuum. In red the measurement without resistor in front of the femto is depicted, in blue the one with resistor. Each time a voltage ramp is applied aconstant current is measurable with the sign dependent on the ramp direction. The applied voltage ramps are from 2 to 20 V/s ascending in 1 V/s steps, ranging from 0 to −500 V.

going back down to 0 V it is positive. The peaks in the current at each leap and over the whole 3 V/s ramp from -500 to 0 V stem from the amplifier as at these points the amplification factor changes. The femto is set up in a way that when the current increases by one magnitude the amplification factor decreases by one. These peaks are therefore not taken into account in the evaluation. Between the measurements without and with resistor no great differences are visible. At approximately 3000 s an offset in time occurs but this is most likely due to an error in the LabVIEW program. For the evaluation, the mean current at each ramp and background is taken. The standard deviation of the mean values is given by

$$\sigma(\bar{x}) = \frac{\sigma(x_i)}{\sqrt{n}} = \sqrt{\frac{\sum_{i=1}^{n}(x_i - \bar{x})^2}{n(n-1)}}, \tag{17}$$

where $\bar{x}$ denotes the mean value, x_i a single value, n the total number of values and

$$\sigma(x_i) = \sqrt{\frac{\sum_{i=1}^{n}(x_i - \bar{x})^2}{n-1}} \tag{18}$$

the standard deviation of a single value to the mean. In addition, each measuring point has an uncertainty of ±50 fA given by the integrated input noise of the femto amplifier. This uncertainty propagates into the mean value according to the Gaussian error propagation

$$\sigma\left(y(x_1, ..., x_i, ...x_n)\right) = \sqrt{\sum_{i=1}^{n}\left(\frac{\partial y}{\partial x_i}\sigma(x_i)\right)^2}. \tag{19}$$

The total uncertainty of the mean value is then given by

$$\sigma_{\text{total}} = \sqrt{\sigma_{\text{syst.}}^2 + \sigma_{\text{stat.}}^2}, \tag{20}$$

where $\sigma_{\text{syst.}}$ denotes the propagated uncertainty derived from the femto and $\sigma_{\text{stat.}}$ the standard deviation of the mean value. For each current at a given ramp, the mean value of the background prior to the ramp is then subtracted from it. Because of the direction reversal of the ramps, this gives now two current values with different signs for each ramp. From the absolute values of these two the average is taken. The resulting current values for the different ramps are shown in fig. 24 for the measurement without and in fig. 25 for the one with resistor. On these values a line according to eq. (15) is fitted. This is done with the SciPy optimize package which uses the least-squares method [33]. The goodness of the fit can be described by the reduced chi-squared statistic:

$$\chi^2_{\text{red}} = \frac{1}{\nu} \sum_{i=1}^{n} \frac{\left(y_i - f(x_i)\right)^2}{\sigma_i^2}. \tag{21}$$

The inputs are the degree of freedom $\nu = n - m$, with n the number of data points and m the number of fitted parameters, the measured value y_i with uncertainty σ_i and the corresponding value $f(x_i)$ of the fit. A fit describes the data well if $\chi^2_{\text{red}} = 1$. If $\chi^2_{\text{red}} > 1$, the fitting model does not match the data or the uncertainty has been underestimated. On the other hand, if $\chi^2_{\text{red}} < 1$ the uncertainty has been overestimated. From the fits a capacitance without resistor of $C^{0\,\Omega}_{\text{vac}} = 265.81\,(4)\,\text{fF}$ is derived with $\chi^2_{\text{red}} = 631$, with resistor a capacitance of $C^{1\,\text{G}\Omega}_{\text{vac}} = 264.63\,(3)\,\text{fF}$ with $\chi^2_{\text{red}} = 42$. The high reduced chi-squared values in both cases are due to the fact that the uncertainty of the measured values is very low and not because the model does not fit the data.

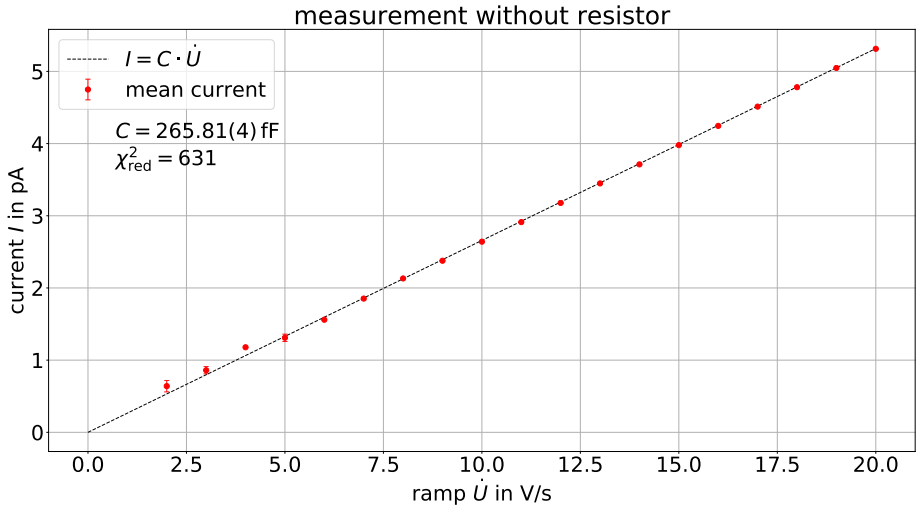

Figure 24: The mean values of the currents at different voltage ramps with a linear fit according to eq. (15) for the measurement without resistor. Errorbars partly smaller than symbols.

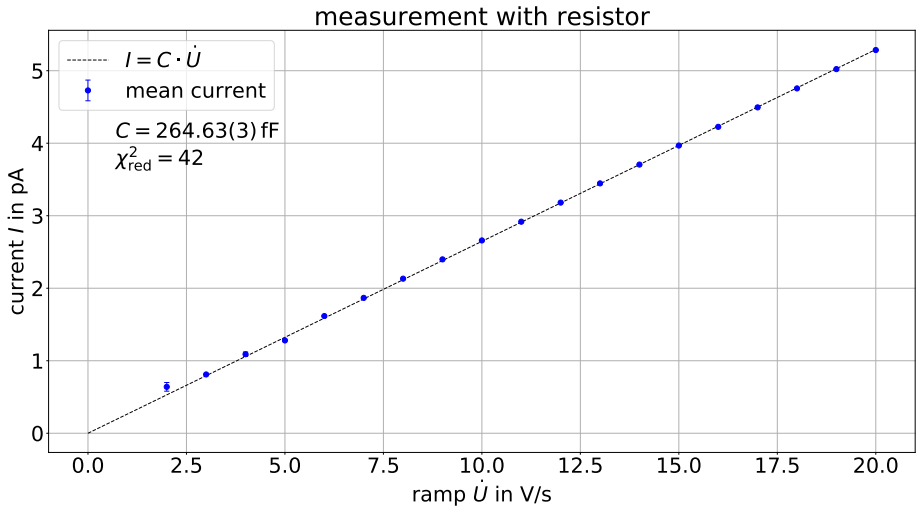

Figure 25: The mean values of the currents at different voltage ramps with a linear fit according to eq. (15) for the measurement with 1 GΩ resistor. Errorbars partly smaller than symbols.

Discussion

Since the derived capacitances of the detector with and without resistor differ only by about 1 fF, it can be said that the additional 1 GΩ resistor has virtually no influence on the measurement. This can be explained by the time constant which, with the derived capacitances, is $\tau \approx 2.6 \times 10^{-4}$ s for the RC element. Since the current is measured at intervals of one second, the charging and discharging processes are already completed on this scale and thus the time constant has no influence on the measurement.
With the measured capacitance it is now also possible to determine the distance between anode and cathode in the detector more precisely. For that, a model of the plate geometry in the detector is built in COMSOL as seen in fig. 26 and a simulation of the Maxwell capacitance is done with varying plate distance. The result of the simulation is shown in fig. 27 with the derived capacitance from the measurement without resistor and its uncertainty also plotted. The simulated capacitance lays at a distance of 2.1803 (3) mm in this interval. Here, the specification of values in the sub-micrometer range is redundant, since the value can change easily in these magnitudes, e.g. due to slight vibrations on the detector. Therefore, it is more safe to say that the plate distance in the detector is 2.18 mm. Comparing this value withe the 2.46 mm measured from outside, the derived value seems plausible.

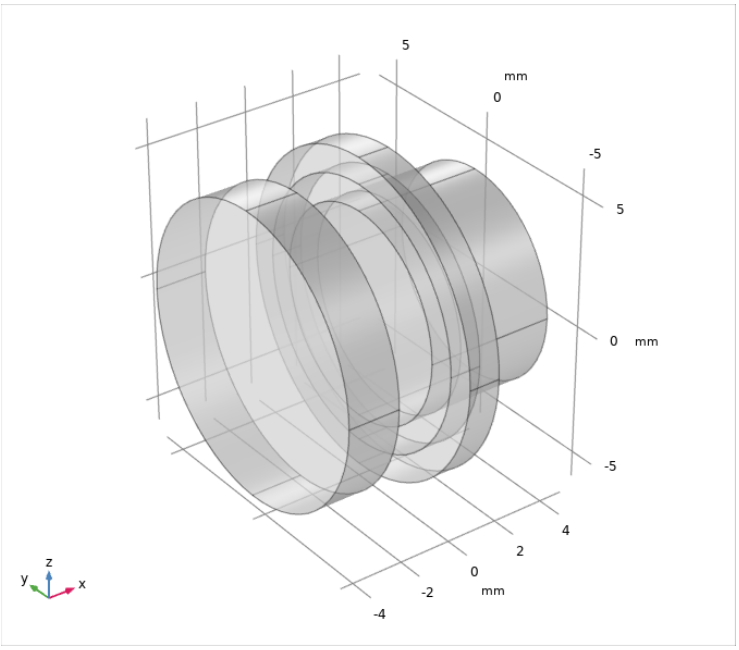

Figure 26: The model of the plate geometry in the detector used in the COMSOL simulations.

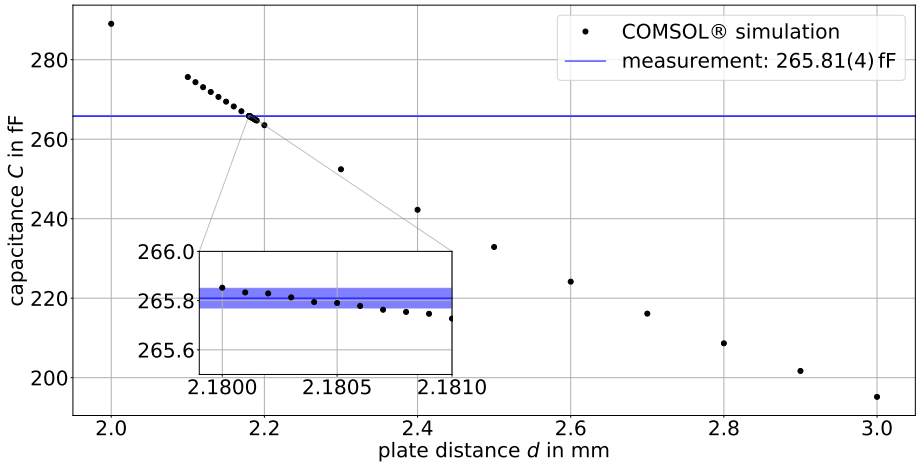

Figure 27: Simulation of the detector capacitance in dependence of the plate distance using COMSOL and the capacitance derived from the current measurements.

5.2 Relative permittivity of TMBi

In TMBi, the current is measured with ramps of 20 to 80 V/s ascending in 10 V/s steps. Due to a high background current and noise, larger ramps than in vacuum are chosen to improve the signal to noise ratio. It is also observed that the background current decreases slowly over time. To reduce the effect of the time dependent background all ramps start from the same initial voltage of −3000 V, which is applied for 9 minutes prior to the first voltage ramp, and go up to −2500 V. Like in the vacuum measurement, the measuring time decreases at higher ramps. After each rise to −2500 V, 200 s of background is measured and after going back down to −3000 V, 400 s is measured. Again, a measuring point is taken every second. The resulting plot is shown in fig. 28.

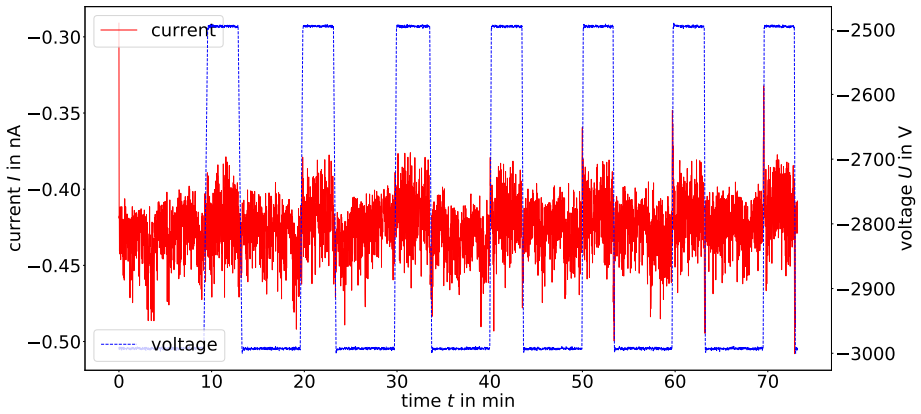

Figure 28: The measured current (red) at the TMBi filled detector and the course of the applied voltage (blue). Voltage ramps from 20 to 80 V/s ascending in 10 V/s steps are applied in the range of -3000 to −2500 V. After a voltage ramp is applied the background current changes.

It can be seen that the background current is around −0.43 nA when −3000 V and rises to approximately −0.41 nA after the voltage changes to −2500 V. For the evaluation only the rising ramps from −3000 V to −2500 V are taken as they can be better distinguished from the background than the falling ramps. To get a mean current for each ramp, first the average background and its standard deviation before and after the ramp is calculated. In addition, the standard deviations of the single values are calculated via eq. (18). This is done to get the standard deviations of the current values while applying the voltage ramp, for which the average between the values before and after the ramp is taken. The ramp currents are then averaged. To subtract the correct background from this mean ramp current, the background before and after the ramp is linearly interpolated using the mean background currents as start and endpoint. The interpolation is done using the form $I = \dot{I} \cdot (t - \bar{t}) + I_0$ with $\dot{I}$ the slope of the line, $\bar{t}$ the middle point of the ramp time and I_0 the y-intercept. This is demonstrated in fig. 29. The mean value of this interpolation, which is the value to subtract from the mean ramp current, is then the current at $t = \bar{t}$ which is equal to I_0. Therefore, in the uncertainty propagation only the uncertainty of the y-intercept I_0 takes part and the slope $\dot{I}$ plays no role.
In fig. 30, the obtained background corrected mean values of the current are plotted against the corresponding ramp. It can be seen that the points seem to follow a lin-

ear course, with exception of the first measuring point at 20 V/s which is slightly shifted upwards. Also the course of the points does not seem to go through the origin, as eq. (15) dictates. Therefore, two linear fits are applied to the points: first according to eq. (15), which can be seen in blue, and second the equation with an added zero current I_0, seen in red. The first fit gives a capacitance of 0.56 (5) fF with a reduced chi-squared of 2.61. According to eq. (16) this results in a relative permittivity of 2.12(19) (the vacuum capacitance measured with resistor is used for the calculation). The reduced chi-squared of 2.61 indicates that this fitting model does not describe the data well. From the second fit one derives a capacitance of 0.99 (13) fF and a zero current of −22 (6) pA with a reduced chi-squared of 0.37, corresponding to a relative permittivity of 3.7(5). Here, the reduced chi-squared indicates that this model describes the data better, but also improperly fits noise due to the large uncertainties of the data. Since no literature value exists for ε_r of TMBi, those values can not be checked.

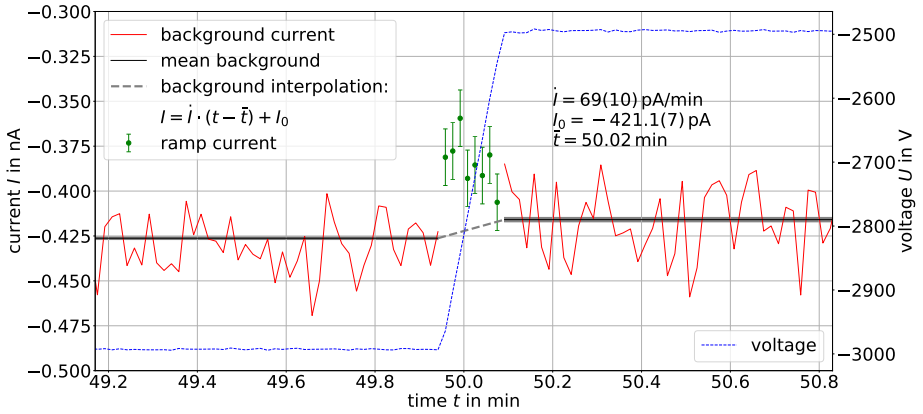

Figure 29: Demonstration of the background interpolation for the 60 V/s ramp. Before and after the voltage ramp is applied the mean (black lines) of the measured background current (red) is calculated. To subtract the correct background from the measured current during the voltage ramp (green), the background is linearly interpolated in this time window (dashed line).

Discussion

As can be seen in fig. 30 and based on the reduced chi-squared values, the fit with the added zero current describes the measurements better than fit solely based on eq. (15). The problem with this approach is that a zero current is not explainable as no current should flow when no voltage is applied to the detector. Another possibility is that eq. (15) can not be applied in this form to the TMBi-filled detector and has to be modified in a way to describe the data. To verify this and the reproducibility of the data, the measurements have to be done again with a larger number of ramps, desirably ramps below 20 V/s to have a better comparison with the vacuum measurements. However, to accomplish this, first the noise needs to be reduced, which would also reduce the uncertainties of the derived values. A possible cause of the noise could be impurities in the TMBi which drift between anode and cathode due to the electric field. These could be extracted from the TMBi through multiple

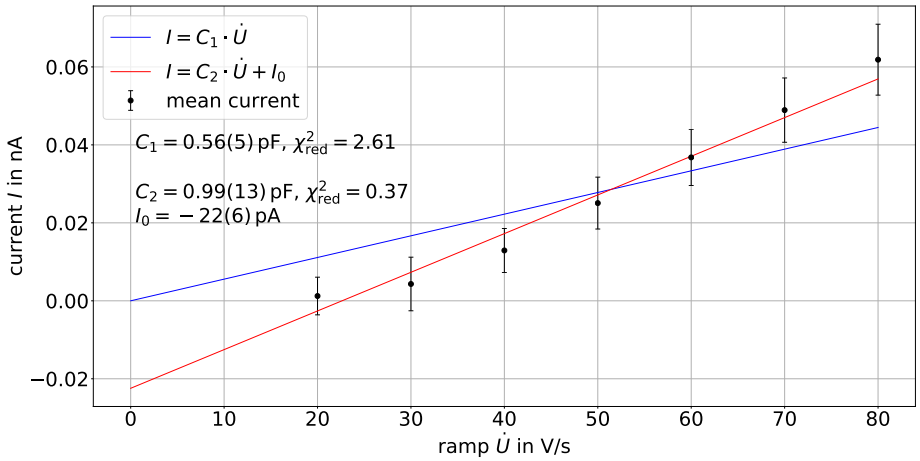

Figure 30: The mean current plotted against the corresponding ramp with a linear fit according to eq. (15) in blue and with a zero current added in red.

cleaning cycles with molecular sieves. The impurities could also be responsible for the time dependency in the background current, as with an applied voltage they slowly drift towards the electrodes and gather there. The background current itself and its change with changing voltage can be explained if the TMBi is not seen as a perfect insulator, but as a resistor. This way a small current flows between cathode and anode dependent on the applied voltage.
If the noise is not a consequence of the impurities and thus can not be reduced by cleaning the liquid, the next step would be the design and assembly of a detector optimized for measurements of the relative permittivity. The detector would then have to have a higher capacitance to deliver a higher current signal, which can be achieved by larger areas of the plates or by a smaller distance between them. To check the functionality of the detector and the measuring method, it should first be filled and tested with a liquid where literature values are known, for example TMSi. This can ensure that no errors are made in determining the relative permittivity of TMBi and an unambiguous result is obtained.

6 Conclusion and outlook

In this bachelor thesis, a liquid ionization detector on the basis of trimethylbismuth was designed and first tested in regard to charge read-out, with the long-term aim to build detectors usable for positron emission tomography.
As the first part of this work, the principles of PET were described in section 2 with main focus on the production, interactions and detection of the 511 keV-photons and the localization of the annihilation through them.
section 3 gives an overview of the working principles of two detector concepts used in PET, scintillation detectors and the liquid ionization detectors. On this occasion the BOLD-PET project and TMBi are introduced.
The design and setup of the new detector are explained in section 4. For this purpose, the requirements on the detector are derived, which are a small TMBi-volume, transparency and argon atmosphere over the TMBi. These conditions are all fulfilled and the TMBi-volume is ultimately less than 9 ml.
Finally, measurements of the current at different voltage ramps are presented in section 5. First, vacuum measurements are done through which the vacuum capacitance of the detector could be calculated to be 265.81 (4) fF without additional resistor and 264.63 (3) fF with a 1 GΩ-resistor in front of the amplifier. Thus, the resistor has no impact on the capacitance. In addition, a COMSOL simulation of the detector geometry is carried out, calculating the capacitance in dependence of the plate distance. The simulation is compared to the derived value without resistor, whereby the plate distance can be determined to be 2.18 mm. This fits in with the 2.46 mm which are measured from outside.
The measurements are also repeated in TMBi. In these measurements, a high noise and background is observed, making the evaluation more difficult. In the end, two values for the capacitance of the TMBi-filled detector can be derived: 0.56 (5) fF through the linear fit that is also used for the vacuum measurement and 0.99 (13) fF with an added zero current. It is seen that the first fit does not describe the data as well as the second fit. From these values and the vacuum capacitance the relative permittivity of TMBi can be calculated which has not been done before in literature. This gives the values 2.12(19) or 3.7(5) respectively.
Due to the high noise, no measurements of the free ion yield in TMBi can be done, since the signal can not be differentiated from it. Therefore, the next step needs to be the reduction of the noise. If it is caused by impurities in the TMBi, this could be done by purifying the TMBi multiple times via molecular sieves. If this is successful, free ion yield measurements can be done using the radioactive source. Furthermore, with reduced noise, the current measurements in TMBi should be repeated to see if the results are reproduceable, to get results with lower uncertainty which mostly stems from the noise and to get measuring points at lower ramps, which could not be measured in this work. This would also help to clarify if the relationship between current and voltage rate is linear or of higher order and thus provide an unambiguous result for the relative permittivity of TMBi.
If the purification of the TMBi does not lower the noise, a new detector model has to be designed. This detector then should have bigger electrodes which would increase the capacitance and therefore the measurable current. Before taking measurements with TMBi the detector should first be tested with a known liquid like TMSi to verify if the detector and the method of measuring provides correct results. If this proves successful, first measurements of the free ion yield in TMBi can be started. With regards to that, it might also be useful to implement a Frisch-grid in the detector. If

the free ion yield is measurable it can be compared with the result of the CaLIPSO-group ([24], see table 2) and then it can be decided if a TMBi-filled detector gives better results than other liquid ionization detectors or if another liquid is more suitable for PET.

A Bibliography

[1] D. Vaughan. *A vital legacy: Biological and environmental research in the atomic age*. Tech. rep. Lawrence Berkeley National Lab., CA, USA, 1997. DOI: 10.2172/305940.

[2] D. Yvon et al. 'CaLIPSO: An Novel Detector Concept for PET Imaging'. In: *IEEE Transactions on Nuclear Science* 61.1 (2014), pp. 60–66. DOI: 10.1109/TNS.2013.2291971.

[3] E. Tiesinga, P. J. Mohr, D. B. Newell and B. N. Taylor. *CODATA Internationally recommended 2018 values of the Fundamental Physical Constants*. Gaithersburg, Maryland, USA: National Institute of Standards and Technology. URL: https://physics.nist.gov/cuu/Constants/index.html (visited on 13/06/2019).

[4] T. Lewellen and J. Karp. 'PET Systems'. In: *Emission Tomography: The Fundamentals of PET and SPECT*. Ed. by M. N. Wernick and J. N. Aarsvold. Elsevier Science, 2004, pp. 179–194. ISBN: 9780080521879. URL: https://books.google.de/books?id=R5slur_hdfEC.

[5] A. Badertscher et al. 'Improved limit on invisible decays of positronium'. In: *Phys. Rev. D* 75 (3 2007), p. 032004. DOI: 10.1103/PhysRevD.75.032004. URL: https://link.aps.org/doi/10.1103/PhysRevD.75.032004.

[6] G. S. Adkins. 'Radiative corrections to positronium decay'. In: *Annals of Physics* 146.1 (1983), pp. 78–128. ISSN: 0003-4916. DOI: https://doi.org/10.1016/0003-4916(83)90053-2. URL: http://www.sciencedirect.com/science/article/pii/0003491683900532.

[7] S. R. Cherry and M. Dahlbom. 'PET: Physics, Instrumentation, and Scanners'. In: *PET: Molecular Imaging and Its Biological Applications*. Ed. by M. E. Phelps. New York, NY, USA: Springer New York, 2004, pp. 1–124. ISBN: 978-0-387-22529-6. DOI: 10.1007/978-0-387-22529-6_1. URL: https://doi.org/10.1007/978-0-387-22529-6_1.

[8] J. H. Hubbell, H. A. Gimm and I. Øverbø. 'Pair, Triplet, and Total Atomic Cross Sections (and Mass Attenuation Coefficients) for 1 MeV-100 GeV Photons in Elements Z=1 to 100'. In: *Journal of Physical and Chemical Reference Data* 9.4 (1980), pp. 1023–1148. DOI: 10.1063/1.555629. eprint: https://doi.org/10.1063/1.555629. URL: https://doi.org/10.1063/1.555629.

[9] H. Krieger. *Grundlagen der Strahlungsphysik und des Strahlenschutzes*. SpringerLink : Bücher. Vieweg+Teubner Verlag, 2012. ISBN: 9783834822383. URL: https://books.google.de/books?id=JjIpBAAAQBAJ.

[10] P. A. Rodnyi. *Physical Processes in Inorganic Scintillators*. Laser & Optical Science & Technology. Taylor & Francis, 1997. ISBN: 9780849337888. URL: https://books.google.de/books?id=BxgNoWH6aPAC.

[11] J. Bleck-Neuhaus. *Elementare Teilchen: Moderne Physik von den Atomen bis zum Standard-Modell*. Springer-Lehrbuch. Springer Berlin Heidelberg, 2010. ISBN: 9783540853008. URL: https://books.google.de/books?id=UzUlBAAAQBAJ.

[12] J. H. Hubbell. 'Review of photon interaction cross section data in the medical and biological context'. In: *Physics in Medicine and Biology* 44.1 (1999), pp. R1–R22. DOI: 10.1088/0031-9155/44/1/001. URL: https://doi.org/10.1088%2F0031-9155%2F44%2F1%2F001.

[13] W. W. Moses, S. E. Derenzo and T. F. Budinger. 'PET detector modules based on novel detector technologies'. In: *Nuclear Instruments and Methods in Physics Research Section A: Accelerators, Spectrometers, Detectors and Associated Equipment* 353.1 (1994), pp. 189–194. ISSN: 0168-9002. DOI: https://doi.org/10.1016/0168-9002(94)91635-7. URL: http://www.sciencedirect.com/science/article/pii/0168900294916357.

[14] T. K. Lewellen. 'Recent developments in PET detector technology'. In: *Physics in Medicine and Biology* 53.17 (2008), pp. R287–R317. DOI: 10.1088/0031-9155/53/17/r01. URL: https://doi.org/10.1088%2F0031-9155%2F53%2F17%2Fr01.

[15] W. W. Moses. 'Fundamental limits of spatial resolution in PET'. In: *Nuclear Instruments and Methods in Physics Research Section A: Accelerators, Spectrometers, Detectors and Associated Equipment* 648 (2011), pp. S236–S240. ISSN: 0168-9002. DOI: https://doi.org/10.1016/j.nima.2010.11.092. URL: http://www.sciencedirect.com/science/article/pii/S0168900210026276.

[16] L. R. MacDonald and M. Dahlbom. 'Parallax correction in PET using depth of interaction information'. In: *IEEE Transactions on Nuclear Science* 45.4 (1998), pp. 2232–2237. ISSN: 0018-9499. DOI: 10.1109/23.708354. URL: https://ieeexplore.ieee.org/document/708354.

[17] P. E. Kinahan, M. Defrise and R. Clackdoyle. 'Analytic Image Reconstruction Methods'. In: *Emission Tomography: The Fundamentals of PET and SPECT*. Ed. by M. N. Wernick and J. N. Aarsvold. Elsevier Science, 2004, pp. 421–442. ISBN: 9780080521879. URL: https://books.google.de/books?id=R5slur_hdfEC.

[18] D. S. Lalush and M. N. Wernick. 'Iterative Image Reconstruction'. In: *Emission Tomography: The Fundamentals of PET and SPECT*. Ed. by M. N. Wernick and J. N. Aarsvold. Elsevier Science, 2004, pp. 443–472. ISBN: 9780080521879. URL: https://books.google.de/books?id=R5slur_hdfEC.

[19] O. Nix. 'Exercises in PET Image Reconstruction'. In: *Molecular Imaging: Computer Reconstruction and Practice*. Ed. by Y. Lemoigne and A. Caner. NATO Science for Peace and Security Series B: Physics and Biophysics. Springer Netherlands, 2008, pp. 131–144. ISBN: 9781402087523. URL: https://books.google.de/books?id=QXUcFrtSOewC.

[20] Hamamatsu Photonics K.K. Hamamatsu, Japan. URL: https://www.hamamatsu.com/eu/en/product/optical-sensors/pmt/about_pmts/index.html (visited on 30/09/2019).

[21] L. Onsager. 'Initial Recombination of Ions'. In: *Phys. Rev.* 54 (8 1938), pp. 554–557. DOI: 10.1103/PhysRev.54.554. URL: https://link.aps.org/doi/10.1103/PhysRev.54.554.

[22] P. de Marcillac, N. Coron, G. Dambier, J. Leblanc and J.-P. Moalic. 'Experimental detection of alpha-particles from the radioactive decay of natural bismuth'. In: *Nature* 422.6934 (2003), pp. 876–878. ISSN: 1476-4687. DOI: 10.1038/nature01541. URL: https://doi.org/10.1038/nature01541.

[23] M. G. Robinson and G. R. Freeman. 'X-Radiolysis Ion Yields and Electron Ranges in Liquid Xenon, Krypton, and Argon: Effect of Electric Field Strength'. In: *Canadian Journal of Chemistry* 51.5 (1973), pp. 641–649. DOI: 10.1139/v73-098. eprint: https://doi.org/10.1139/v73-098. URL: https://doi.org/10.1139/v73-098.

[24] M. Farradèche et al. 'Free ion yield of trimethyl bismuth used as sensitive medium for high-energy photon detection'. In: *Journal of Instrumentation* 13.11 (2018), P11004–P11004. DOI: 10.1088/1748-0221/13/11/p11004. URL: https://doi.org/10.1088%2F1748-0221%2F13%2F11%2Fp11004.

[25] R. L. Amey and R. H. Cole. 'Dielectric Constants of Liquefied Noble Gases and Methane'. In: *The Journal of Chemical Physics* 40.1 (1964), pp. 146–148. DOI: 10.1063/1.1724850. eprint: https://doi.org/10.1063/1.1724850. URL: https://doi.org/10.1063/1.1724850.

[26] J. Engler and H. Keim. 'A liquid ionization chamber using tetramethylsilane'. In: *Nuclear Instruments and Methods in Physics Research* 223.1 (1984), pp. 47–51. ISSN: 0167-5087. DOI: https://doi.org/10.1016/0167-5087(84)90245-X. URL: http://www.sciencedirect.com/science/article/pii/016750878490245X.

[27] COMSOL AB. *COMSOL Multiphysics®*. Version 5.4. Stockholm, Sweden. URL: www.comsol.com.

[28] Leybold GmbH. Köln, Germany. URL: https://www.leyboldproducts.de/media/pdf/25/13/a0/180_85_01_PHOENIX_L300i_DE.pdf (visited on 28/10/2019).

[29] Pfeiffer Vacuum GmbH. Asslar, Germany. URL: https://www.pfeiffer-vacuum.com/de/produkte/messung-analyse/analysegeraete/restgasanalyse/restgasanalyse-im-ultrahochvakuum/prismapro-qmg-250-m3-1-300-u/32111/prismapro-qmg-250-m3-1-300-u (visited on 15/10/2019).

[30] LAUDA DR. R. WOBSER GMBH & CO. KG. Lauda-Königshofen, Germany. URL: https://www.lauda.de/de/temperiergeraete/thermostate/kaeltethermostate/eco.html (visited on 29/10/2019).

[31] iseg Spezialelektronik GmbH. Radeberg, Germany. URL: https://iseg-hv.com/en/products/detail/NHQ (visited on 10/10/2019).

[32] FEMTO® Messtechnik GmbH. Berlin, Germany. URL: https://www.femto.de/en/products/current-amplifiers/sub-femto-ampere-var-gain-ddpca.html (visited on 10/10/2019).

[33] P. Virtanen et al. 'SciPy 1.0–Fundamental Algorithms for Scientific Computing in Python'. In: *arXiv e-prints*, arXiv:1907.10121 (2019), arXiv:1907.10121. arXiv: 1907.10121 [cs.MS].